Investigation of red blood cell properties on impedance signatures generated in a Coulter counter

Pierre Pottier, Pierre Taraconat, Jean-Philippe Gineys, Damien Isebe, Franck Nicoud, Simon Mendez

Received: Added at production | Revised: Added at production | Accepted: Added at production

DOI: xxx/xxxx

ARTICLE TYPE

Investigation of red blood cell properties on impedance signatures generated in a Coulter counter

Pierre Pottier[1,2] | **Pierre Taraconat**[1] | **Jean-Philippe Gineys**[1] | **Damien Isèbe**[1] | **Franck Nicoud**[2,3] | **Simon Mendez**[2]

[1]HORIBA ABX SAS, 398 rue du Caducée, 34790 Grabels, France

[2]Institut Montpellierain Alexander Grothendieck, CNRS, Univ. Montpellier, 2 Place Eugene Bataillon, 34095 Montpellier Cedex 5, France

[3]Institut Universitaire de France, IUF, France

Correspondence
Simon Mendez
Email: simon.mendez@umontpellier.fr

Funding Information
This research was supported by the Text

JEL Classification: ejlje

Abstract

The ability of red blood cells (RBCs) to deform is essential for microcirculation and oxygen delivery. Any changes in RBC deformability can lead to significant cardiovascular complications, necessitating timely detection. Although specialized microdevices can be designed to assess RBC deformability, leveraging instruments already used in clinical settings would enable easier integration and accelerate clinical translation. Coulter counter (CC) systems are routinely used to count, size, and analyze RBCs and the possibility to extend their diagnostic capabilities to RBC deformability is currently examined. In this study, the effects of RBCs geometrical, morphological and rheological properties on CC measurement have been investigated numerically, thanks to a simulation framework predicting the RBC dynamics in a CC and the associated impedance signature. Subsequently, a numerical parametric study has been performed and the resulting pulses have been compared with experimental results, confirming the simulation's accuracy in predicting CC measurements. In addition to the RBC volume and the RBC trajectory in the sensing region, which had been investigated before, present results show that in our modeling framework, RBC sphericity, membrane viscosity, and cytoplasm viscosity are the main RBC characteristics contributing to the broad CC measurement spectrum observed experimentally when analyzing healthy blood samples.

KEYWORDS
Red blood cell, Coulter counter, Computational Fluid dynamics, Mesh adaptation

1 | INTRODUCTION

Healthy red blood cells (RBCs) have the property to significantly change their shape under external stresses. Their high deformability plays a key role in blood circulation and oxygen delivery, especially in microcirculation where RBCs circulate through capillaries narrower than their size at rest [1]. Moreover, severe cardiovascular dysfunction can occur when the deformability of RBCs is impaired. For example, anemias, organ ischemia or hypertension may develop in patients with pathologies affecting RBC deformability such as spherocytosis [2,3], sickle cell disease [4,5] or diabetes mellitus [1,6]. The detection of abnormal RBC deformability is thus crucial for predicting and preventing major cardiovascular complications. Among the methods used for measuring RBC deformability at the single cell level, the manual micropipette [7,8], optical tweezers [9,10] and atomic force microscopy [11,12] are among the most widely used. High-throughput automated techniques are also available, such as ektacytometry [3,13] and microfluidic systems [14,15]. To the best of our knowledge, none of these methods are implemented in routine analysis, although they can be employed for specific diagnostic purposes [16,17].

A routine and widely used blood test is the complete blood count (CBC), which includes RBC count and size. Figures 1a–1c illustrate the principle of an automated electric impedance-based system, the Coulter counter (CC) [18], commonly used for this purpose. In a CC, RBCs are diluted and suspended in an electrolyte reagent in a tank presented in Figure 1a, then drawn through a micro-orifice shown in Figure 1b. Electrodes on either side of the micro-orifice generate an electric field in the system. When the RBCs flow through the orifice, they cause a variation in the electric resistance of the system, referred to as

Abbreviations: CC, Coulter counter; CBC, complete blood count; FSI, Fluid-structure interaction; IBM, immersed boundary method; MA, mesh adaptation RBC, red blood cell

"pulse". This mechanism is illustrated in Figure 1b, showing two particles (in different colors) following distinct trajectories. The corresponding electric perturbations are presented in Figure 1c, with colors consistent with those of the associated particles. To ensure high throughput, RBCs travel through the orifice at speeds of several meters per second, with pulse durations on the order of tens of microseconds.[19].

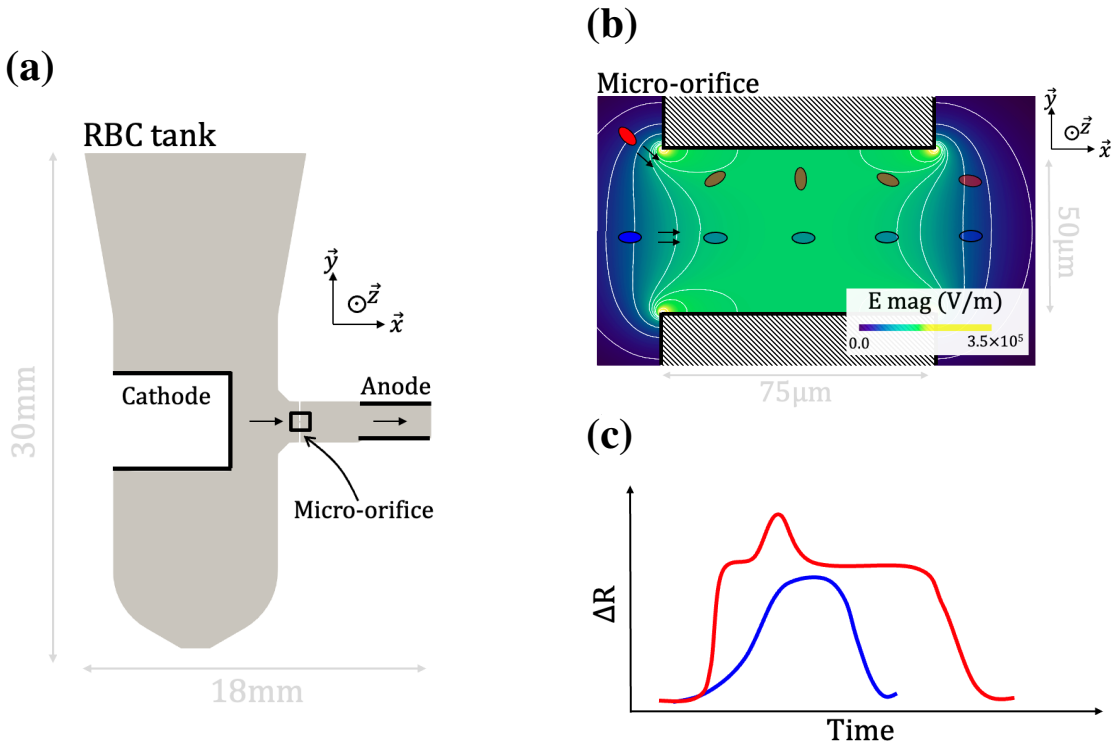

FIGURE 1 Coulter principle illustrated with a schematic version of the ABX Micros 60 (HORIBA) analyzer. (a) Slice cut of RBC tank. The electrodes are highlighted with black solid lines, positioned on each side of a rectangle that indicates the location of the cylindrical orifice. (b) Slice cut of the micro-orifice. The electric field magnitude is mapped on the micro-orifice picture (cell-free). Electric field isolines are shown with white lines. The blue and red dots illustrate the time-lapse positions of two different RBC moving through the orifice, with different trajectories. (c) Time evolution of the electric perturbations associated with the passage of RBCs through the micro-orifice. The blue pulse represents the electric perturbation caused by the blue particle (central path), while the red pulse corresponds to the red particle (near-wall path).

Consistent with experimental observations, the following relation has been proposed by Kachel *et al.*[20] to assess a resistive pulse ΔR for an insulating particle flowing in a CC:

$$\Delta R \propto f_s V, \tag{1}$$

where V is the volume of the particle and f_s a shape factor that accounts for the particle size, orientation and shape. Focusing on hydrodynamical effects, it has been shown that non-spherical particles exhibit different dynamics depending on their proximity to the wall, resulting in varying pulse shapes for the same particle[19,21]. Particles flowing in the central region (blue particle in Figure 1b) remain aligned with the flow direction and generate standard bell-shaped pulses (blue pulse in Figure 1c), whose maximum amplitude is used as a measurement of cell volume[20]. In contrast, particles flowing near the orifice wall (red particle in Figure 1b) are subjected to strong shear forces, causing them to rotate and deform, which yields an additional peak occurring during cell rotation (red pulse in Figure 1c). This "rotation peak", which increases the pulse's maximum amplitude, is induced by an increase of f_s[19,20]. In systems where these types of artifacts occur, the measured volume distribution is abnormally skewed to the right and fails to accurately represent the true statistics of RBCs volume[22]. Various strategies have been proposed to correct

volume distribution, including hydrofocused systems, that force RBCs to pass through the central region of the orifice[23], or pulse editing strategies, designed to filter out near-wall pulses[22,24].

Recent studies demonstrated the sensitivity of pulses with a rotation peak to RBC deformability: Taraconat *et al.*[25] showed that the rotation peak increases if the RBC is rigidified, or is practically nonexistent if the RBC is spherized. These results have been confirmed experimentally with analyses conducted on artificially modified RBCs[25]. In addition, the pulses with rotation peak have been used to discriminate healthy blood samples from pathological blood samples containing RBCs with altered deformability[6].

In the long term, the objective is to enhance CC diagnostic capabilities by identifying morphological and rheological RBC properties from the CC measurements. However, the relationship between the RBCs characteristics and the impedance signatures has not been fully elucidated. Indeed, the numerical study conducted by Taraconat *et al.*[25] considered a simplified model for the RBC, in which RBC membrane viscosity was neglected. However, RBC membrane viscoelasticity is expected to play an important role in such configurations, where RBCs are subjected to rapid variations of stress. The role of RBC initial orientation in the RBC tank (before the vacuuming phase) was not discussed either. Of course, interpreting the impedance signatures in terms of RBC characteristics and dynamics requires: (1) identifying all factors responsible for variations in pulse shape, and (2) ensuring that numerical simulations can reproduce the pulse variations observed experimentally.

This study focuses on the two prerequisites outlined above. To do so, we propose a numerical approach to explore how the geometrical, morphological, and rheological properties of RBCs, including the viscosity of the RBC membrane and their initial orientation, influence resistance pulses. The numerical framework is based on the work of Taraconat *et al.*[19], enhanced with a mesh adaptation (MA) strategy for improving computation efficiency. First, the numerical framework and the experimental set up are presented in section 2. Following the numerical model's validation in section 3.1, the influence of RBCs properties is investigated through a one-at-a-time sensitivity analysis at multiple operating points in section 3.2. Subsequently, a numerical systematic parametric study has been performed with all RBC properties identified, and the results are compared with experimental data in section 3.3. Finally, the model's ability to capture the experimental pulses are discussed in section 4.

2 | MATERIALS & METHODS

2.1 | Numerical simulations

Simulations are performed with YALES2BIO (http://imag.umontpellier.fr/~yales2bio), a numerical simulation software dedicated blood flow simulations at different scales[26]. Predicting impedance pulses in a CC first necessitates to solve a fluid-structure interaction (FSI) problem involving the RBC and the ambient fluid. Then, the resistive pulses associated with the RBC dynamics can be computed. In a real device, the blood samples are sufficiently diluted so that RBCs flow in the micro-orifice one after the other. Coincident passages can easily be filtered. We thus focus on the case of an isolated RBC with variable properties flowing in a CC. The model and the numerical method for both the FSI and the electric problems are summarized in section 2.1.1. A mesh adaptation strategy is proposed to reduce the computational cost of the simulation in section 2.1.2. Section 2.1.3 summarizes the pipeline.

2.1.1 | Modeling framework

Fluid-structure interaction calculation

Predicting the dynamics of an RBC in a CC requires solving a fluid–structure interaction problem between the incompressible suspending electrolyte and the RBC. The latter is modeled as a droplet of Newtonian fluid (the cytoplasm) enclosed by an infinitely thin, deformable solid structure representing the membrane. The volume of the RBC V_{RBC} is fixed (the membrane is assumed impermeable) and the surface at rest is denoted by S_{RBC}. As the lipid bilayer is quasi-incompressible, S_{RBC} also remains constant. This allows to define Q, the sphericity index, as: $Q = \frac{V_{\mathrm{RBC}}}{V_{\mathrm{sphere}}}$, with V_{sphere} the volume of a sphere having the same surface area as the RBC, S_{RBC}. For a given surface, a larger RBC volume results in a more spherical cell, with Q approaching 1.0. On the other hand, Q tends to 0 when the RBC is emptied of its volume and adopts a flattened shape.

From a mechanical point of view, the RBC membrane resists different types of stresses, in particular shear and area changes, modeled here with Skalak's hyperelastic law[27]:

$$W_{\mathrm{SK}} = \frac{G_s}{4}[(\lambda_1^2 + \lambda_2^2 - 2) + 2(\lambda_1^2 + \lambda_2^2 - \lambda_1^2\lambda_2^2 - 1)] + \frac{E_a}{4}(\lambda_1^2\lambda_2^2 - 1). \tag{2}$$

W_{SK} is the strain energy of the membrane. It is a function of the principal in-plane strain values (λ_1 and λ_2), the shear modulus G_s and the area-change modulus E_a. The bending resistance of the membrane is described by the Helfrich bending energy ε_b [28]:

$$\varepsilon_b = \frac{E_b}{2}\int_S (2\kappa - C_0)^2 dS. \tag{3}$$

E_b the bending modulus, κ the mean curvature and C_0 the spontaneous curvature.

In addition, the RBC membrane has been shown to have a viscoelastic behavior [29,30]. In YALES2BIO, membrane viscosity is considered through Skalak's law [31], in which the classical shear modulus G_s of Eq. 2 is replaced by a relaxation modulus $E_r(t)$:

$$E_r(t) = G_s + E_e e^{-\frac{t}{t_c}}, \tag{4}$$

where t_c refers to a characteristic time, computed as: $t_c = \frac{\eta_{memb}}{E_e}$, with η_{memb} the membrane viscosity. In practice, E_e is set to $E_e = 50G_s$ [31] to have negligible differences with a Kelvin-Voigt model, which is the classical model used to characterize membrane viscosity [29,14]. However, the implementation through a Zener model (Eq. 4) is preferred here for stability reasons [31,32]. As generally assumed in simulations of RBC dynamics, membrane viscosity only resists shear stresses (not area changes). The relaxation modulus $E_r(t)$ is thus included in Skalak's law solely for computing the deviatoric part of the stress tensor [31]. The model does not account for potential stress-induced RBC damage [33,34]; therefore, RBC properties remain constant throughout each simulation.

The fluid is assumed to be incompressible and Newtonian. The flow is thus governed by the incompressible Navier-Stokes equations, solved on an Eulerian mesh consisting of tetrahedral elements. The RBC membrane is modeled using a two-dimensional Lagrangian mesh composed of triangular elements. FSI calculations are carried out using the immersed boundary method (IBM) originally developed by Peskin *et al.* [35], extended to unstructured grids using the Reproducing Kernel Particle Method (RKPM) [36,26]. At each time step, RBC membrane forces are calculated from the membrane deformation and the behavior laws (Eqs. 2 - 4) [37,38,31]. Then, membrane forces are regularized over the fluid domain using the RKPM [26]. In addition, the viscosity field is recalculated at each time step at the fluid grid vertices, based on the position of the membrane, in order to assign the cytoplasm viscosity inside the membrane and the electrolyte viscosity outside. The Navier-Stokes equations are thus written as follows:

$$\frac{\partial \vec{u}}{\partial t} + \vec{u}\cdot\nabla\vec{u} = -\frac{\nabla P}{\rho} + \nabla\cdot[\nu(\nabla\vec{u} + (\nabla\vec{u})^t)] + \vec{f}, \tag{5}$$

$$\nabla\cdot\vec{u} = 0, \tag{6}$$

with $\vec{u}$ the fluid velocity, ν the fluid kinematic viscosity (which varies in space), ρ the fluid density and P the pressure. $\vec{f}$ is a source term that represents the effect of RBC membrane forces on the fluid. In the rest of this paper, the kinematic viscosity is denoted by ν_{in} inside the RBC and ν_{ext} in the suspending medium. Eq (5) is discretized with a fourth-order finite-volume method, and advanced in time with a fourth-order Runge-Kutta scheme. The resolution of the velocity field is achieved thanks to the prediction-correction method from Chorin *et al.* [39] predicting a velocity field with the previous pressure term, then correcting it based on the pressure Poisson equation (enforcing incompressibility condition). The pressure Poisson equation is solved using a Deflated Preconditioned Conjugate Gradient [40]. Once the velocity field has been calculated on the fluid grid, it is interpolated onto the vertices of the membrane mesh and the RBC membrane is advanced in time with an explicit Euler scheme.

The FSI framework is used to predict the dynamics of an RBC circulating through a CC and needs to be completed by an electric calculation to obtain the associated pulse.

Electrostatic calculation

The CC measurement consists in the time-dependent variation in the electric resistance of the system during the passage. A separate set of computations is therefore carried out to evaluate the resistance change, $\Delta R(t)$, associated with an RBC flowing

through the micro-aperture: $\Delta R(t) = R_{\mathrm{RBC}}(t) - R_{\mathrm{CF}}$. R_{CF} is the resistance computed in a cell-free configuration, and $R_{\mathrm{RBC}}(t)$ is the resistance of the system perturbed by an RBC, at time t. The RBC is assumed to be perfectly insulating, which is mimicked in the IBM framework by setting the conductivity inside the RBC σ_{in} to 0. Furthermore, the effects of the electric field on RBCs dynamics are neglected and it is assumed that the electric field develops instantaneously. In this respect, electric effects are decoupled from FSI problem and disturbances caused by an RBC over time may be seen as a series of electrostatic problems to be solved. For each RBC state (defined by its position in the device, shape and orientation), an electrostatic equation based on Maxwell–Ampere's law is solved to compute the potential ψ_{RBC}. The cell-free potential ψ_{CF} is also computed:

$$\nabla \cdot (\sigma_{ext} \nabla \psi_{\mathrm{CF}}) = 0, \tag{7}$$

$$\nabla \cdot (\sigma_{var}(t) \nabla \psi_{\mathrm{RBC}}(t)) = 0. \tag{8}$$

σ_{ext} is the conductivity of the suspending medium. $\sigma_{var}(t)$ is the time-dependent conductivity field, equal to σ_{ext} outside the RBC and σ_{in} inside. Once Eqs. 7 - 8 are solved, the potential gradient is computed to obtain the electric field $\vec{E}$. Then, $\vec{E}$ is integrated over the orifice surface entrance S to calculate the resistance R, knowing the applied potential between the two electrodes, U:

$$R = \frac{U}{\int_S \sigma \vec{E} \cdot d\vec{S}}, \qquad with\, \vec{E} = \nabla \psi. \tag{9}$$

Parametric study

In this study, the device and its operating conditions are fixed, with unchanged geometry, flow rate, and electrode potential. A sensitivity analysis is performed to examine how RBC geometry, mechanical properties, and position/orientation affect the results. Simulations use RBC properties characteristic of healthy cells, Table 1 providing typical parameter ranges from the literature.

TABLE 1 Typical values of morpho-rheological properties for healthy RBCs, found in the literature, along with possible ϕ-orientations in the CC. The values tested in the parametric study are also specified.

Parameter name	Parameter bounds ([min, max])	Tested values
Shear modulus G_s (μN.m^{-1}) [7,8,10]	[2.2, 22.5]	2.2, 12.4, 22.5
Internal visosity ν_{in} (10^{-6} m^2.s^{-1}) [41,42,43]	[7.0, 15.0]	7.0, 11.0, 15.0
Sphericity index Q [44,45,46]	[0.57, 0.78]	0.57, 0.68, 0.78
Membrane viscosity η_{memb} (Pa.m.s) [31,29,47]	[3.0×10^{-8}, 1.0×10^{-6}]	0, 5.0×10^{-9}, 2.5×10^{-8}
Change area modulus E_a (N.m^{-1}) [19,25,48]	[0.238, 0.338]	0.25
Bending modulus E_b (J) [19,25,49]	[3.0×10^{-19}, 8.0×10^{-19}]	6.0×10^{-19}
ϕ orientation	[0, $\frac{\pi}{2}$]	0, $\frac{\pi}{4}$, $\frac{\pi}{2}$

In the industrial device, the micro-orifice is cylindrical and the flow field is axisymmetric around the central axis of the orifice [19]. Without loss of generality, we consider an RBC whose center of mass lies in the $(\vec{x}, \vec{y})$ plane shown in Figure 1a. In this study, we will consider a unique trajectory to focus our attention on the other parameters of the RBC (orientation, shape and mechanics). The dependence of the pulse on the trajectory has been studied previously [19,25].

Across the RBC tank (upstream the orifice), the RBCs are subjected to axisymmetric extensional flow along their trajectory [19,20]. The RBCs are reoriented by the flow and their minor axis, shown in Figure 2a, tends to be orthogonal to the trajectory before entering the orifice [20,50]. The initial angle between the RBC minor axis and its trajectory in the RBC tank, denoted by θ, is illustrated in Figures 2a - 2b. Due to the reorientation by the flow, it is assumed to have negligible effect on pulses and is therefore initialized to $\frac{\pi}{2}$. Except for θ orientation, the upstream flow does not impose any other constraint on RBC orientation. Therefore, the initial angle formed between the RBC minor axis and the plane $(\vec{x}, \vec{y})$, called ϕ, has been included in the factors that may impact RBCs dynamics in the orifice. Figures 2a and 2c illustrate RBC ϕ orientation. Note that ϕ was not mentioned in the work of Taraconat *et al.* [25], in which it had been fixed to 0.

In the simulations, we fixed S_{RBC} to a typical value of 133.4 μm^2. The volume of the RBC then varies linearly with Q. The mechanical moduli E_a and E_b have been set to 0.25 N.m^{-1} and 6.0×10^{-19} J, respectively. The spontaneous curvature of

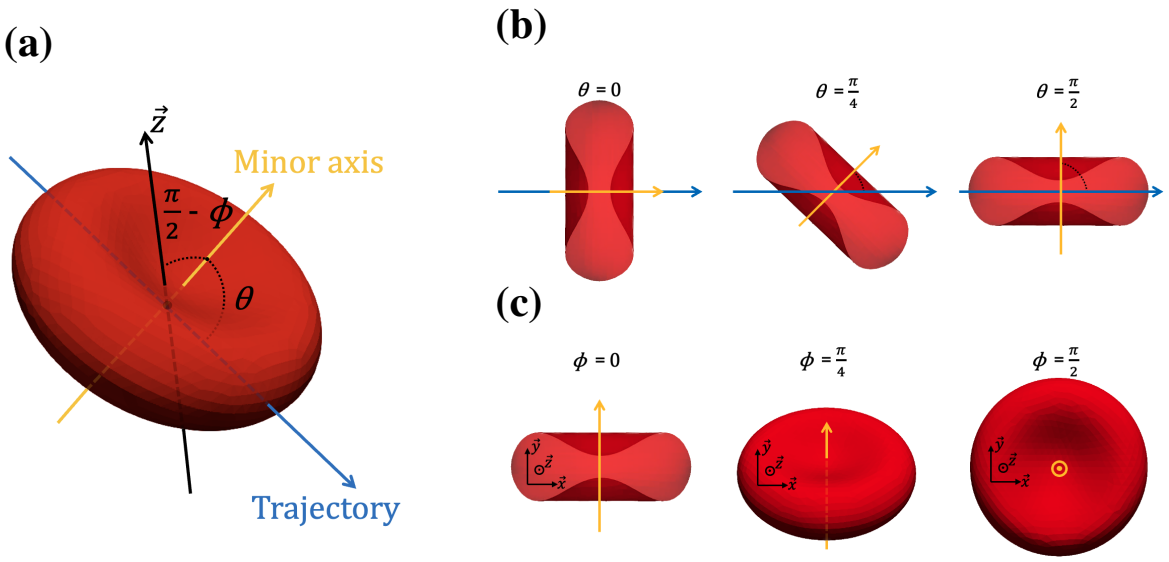

FIGURE 2 Discocyte RBCs with different orientation. The orientation of an RBC is characterized by θ and ϕ, the angle of the RBC minor axis relative to the RBC trajectory, and the angle relatively to the $(\vec{x}, \vec{y})$ plane. (a) An RBC with a sphericity index $Q = 0.65$. The yellow arrow designates the RBC minor axis. The blue arrow corresponds to the RBC trajectory, while the black arrow designates $\vec{z}$ axis from the coordinate system presented Figure 1a. (b) RBCs with various θ orientation. (c) RBCs with various ϕ orientation.

RBC membrane has been fixed to $C_0 = 0\ \mathrm{m}^{-1}$ in this study. Varying this value could be particularly interesting for studying non-discocyte RBC shapes, such as stomatocytes or echinocytes[51].

A numerical parametric study was conducted involving G_s, ν_{in}, Q (and thus the RBC volume), ϕ, and η_{memb}. For each parameter, three levels were defined representing the lowest, mid-range, and highest values reported in the literature for healthy RBCs (see Tested values in Table 1). Note however that the range of η_{memb} from the literature is very large, spanning two orders of magnitude. We decided to explore several values and present the results for $\eta_{memb} = 0$ (no membrane viscosity), 5×10^{-9} Pa.m.s, and 25×10^{-9} Pa.m.s. It is worth noting that the highest value tested is lower than those reported for normal RBCs in the literature. This will be further commented in section 4.

2.1.2 | Meshing and dynamic mesh adaptation

As already mentioned, the surface area of the RBC membrane is here a fixed parameter: $S_{\mathrm{RBC}} = 133.4\ \mu\mathrm{m}^2$. The membrane is discretized with elements of size $h_{\mathrm{RBC}} = 0.3\ \mu$m, (which corresponds to approximately 4000 faces and 2000 nodes for one RBC). In the IBM, the best accuracy is obtained when the fluid grid size is similar to that of the membrane[26]. As a consequence, the fluid grid size near the cell must be approximately 0.3 µm. Unstructured grids allow to coarsen the grid far from the cell. In previous works[19,25], the fluid grid size was set to h_{RBC} over the whole RBC trajectory and this grid was static during the whole simulation.

We introduce a dynamic MA method for simulating RBC dynamics in the CC, which refines the grid locally around the RBC as it moves. The method relies on remeshing: the fluid grid is held fixed until a specified criterion is reached, at which point a new grid is generated with a prescribed mesh size across the domain. We first detail how the mesh size is defined at remeshing, and then present the criterion used to trigger the MA process.

Theoretical definition of the mesh size

The method starts from a baseline grid, obtained by mesh convergence for the cell-free fluid flow, with grid size $h_0(\vec{x})$. In this work, $h_0(\vec{x})$ is larger then h_{RBC}, the membrane mesh size and target grid size in the IBM framework. We thus define a volume Ω_{IBM} around the RBC, within which the grid size h_{RBC} is imposed. This volume is chosen to be cylindrical. Figure 3a displays Ω_{IBM} in an example, with its characteristics detailed later. Once Ω_{IBM} is defined, the target grid size is expressed as a function of h_{RBC}, $h_0(\vec{x})$ and a blending function $\alpha(\vec{x})$:

$$h(\vec{x}) = \alpha(\vec{x})\, h_{\mathrm{RBC}} + (1 - \alpha(\vec{x}))\, h_0(\vec{x}), \text{ with } \begin{cases} \alpha(\vec{x}) = 1, & \text{if } \vec{x} \in \Omega_{\mathrm{IBM}}, \\ \alpha(\vec{x}) \in [0, 1[\text{ such that } \nabla h(\vec{x}) < \nabla h_{\max}, & \text{if } \vec{x} \notin \Omega_{\mathrm{IBM}} \end{cases} \tag{10}$$

Besides applying a mesh size of h_{RBC} within the refined region Ω_{IBM} (where $\alpha(\vec{x}) = 1$), $\alpha(\vec{x})$ must be kept as close to 0 outside Ω_{IBM}, so that the mesh size tends toward the background mesh size $h_0(\vec{x})$. However, $\alpha(\vec{x})$ is modulated by the gradient of the mesh size $h(\vec{x})$ to avoid abrupt variations in element size. Following Grenouilloux *et al.*[52], the mesh gradient $\nabla h(\vec{x})$ must not exceed a maximum threshold $\nabla h_{\max} = 0.3$. Accordingly, $\alpha(\vec{x})$ is defined as the smallest positive value that ensures the condition $\nabla h(\vec{x}) \leq 0.3$ throughout the domain.

Naturally, Ω_{IBM} must fully encompass the RBC. Moreover, to minimize the frequency of remeshing, this region is extended to include the cell's anticipated future positions. To achieve this, we assume that the RBC's future positions can be reasonably estimated using its mean velocity at the time of remeshing, $\overrightarrow{u_{\mathrm{RBC}}}$. We first define the so-called core region as the smallest cylinder, with its axis aligned with the cell's mean velocity, that fully encloses the RBC. Its axis length and radius read:

$$l_c = \max_i \overrightarrow{\widehat{u}_{\mathrm{RBC}}} \cdot \overrightarrow{X_i} \; + \; | \min_i \overrightarrow{\widehat{u}_{\mathrm{RBC}}} \cdot \overrightarrow{X_i} \; | \tag{11}$$

$$r_c = \max_i \sqrt{\left\| \overrightarrow{X_i} \right\|^2 - (\overrightarrow{\widehat{u}_{\mathrm{RBC}}} \cdot \overrightarrow{X_i})^2} \tag{12}$$

$\overrightarrow{X_i}$ designates the vector connecting the RBC centroid to the membrane grid node X_i, and $\overrightarrow{\widehat{u}_{\mathrm{RBC}}}$ is a unit vector directed by $\overrightarrow{u_{\mathrm{RBC}}}$.

That cylinder is then extended in the direction of the velocity vector by a length l_{ext}. Additionally, because the RBC is generally subjected to shear-induced rotation, the cylinder's radius is further extended by r_{ext} to ensure that the cell remains within the fine region despite rotational motion. This prevents premature exit from the refined mesh zone. Figure 3b illustrates Ω_{IBM} sizing details with the core-region bounded by a blue rectangle, and the entire fine region bounded with a black rectangle. Note that l_{ext} and r_{ext} are user-defined parameters. Their effect will be tested in section 3.1.

Practical definition of the mesh size for the use of the remeshing library MMG3D

In order to perform the MA, YALES2BIO is coupled with MMG3D[53,54], a library for the adaptation and the optimization of tetrahedral meshes. MMG3D remeshes the existing grid using a metric field, which, in the case of isotropic meshing, defines the local target element size. This metric field is defined at each node of the previous fluid grid. In order to impose the grid size h_{RBC} in the fine region, it is prescribed that for all grid elements intersecting the cylinder describing the fine region, the vertices of the elements have a metric value of h_{RBC}. The edge lengths of the grid are adjusted by MMG3D to match the desired size, either through edge splitting or collapsing, or by inserting nodes followed by an update of the connectivity. Further information on the MMG3D remeshing algorithm and its integration into YALES2BIO can be found in the relevant literature[52,53,54,55].

Criterion for remeshing

The criterion that governs when the remeshing process is triggered remains to be specified. At each iteration, the positions of all membrane mesh vertices are compared with the boundaries of the fine region defined during the previous remeshing. If any membrane node lies within a distance less than h_{RBC} from the boundary of this region, a new fine region is then defined around the RBC and remeshing is triggered. This ensures that the RBC remains entirely within a portion of the grid that satisfies the resolution required by the IBM. The new fine region necessarily overlaps with the previous one. In this overlapping region, the existing mesh already satisfies the prescribed remeshing metric. The remeshing algorithm is instructed to preserve the previous grid in this area, so that no interpolation is required in the critical region surrounding the RBC.

Remeshing algorithm

The remeshing algorithm can be summarized as follows. It starts from a grid with an associated fine region Ω_{IBM} and a given RBC position.

1. At each iteration, the FSI system is solved and the RBC position is updated
2. A remeshing trigger test is performed to determine whether the RBC is close enough to the boundaries of the fine region Ω_{IBM}. If not, the next iteration proceeds. Otherwise, remeshing is initiated.
3. A new fine region is defined by first calculating the center of mass and the mean velocity of the RBC. The core region of length l_c and radius r_c is constructed around the RBC. This core is then extended based on user-defined parameters l_{ext} and r_{ext} to form the new fine region.

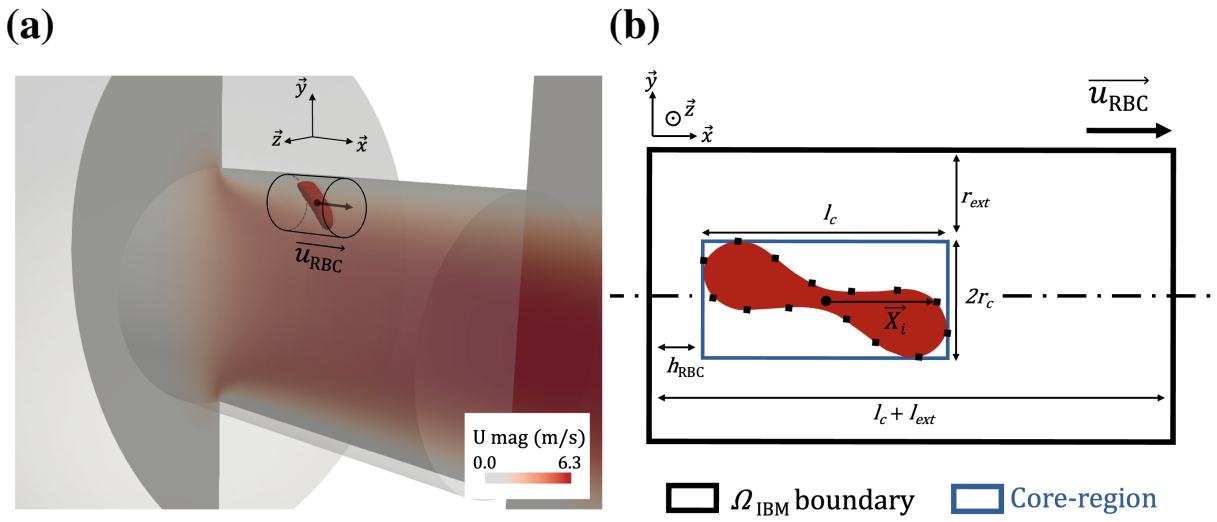

FIGURE 3 Illustration of the fine region Ω_{IBM}. (a) Example of Ω_{IBM} region with a black cylinder for an elongated RBC in a micro-orifice (colored with the fluid velocity field). Black arrows designate then $\overrightarrow{u_{\text{RBC}}}$ direction. (b) Schematic example (in 2D) of Ω_{IBM} detailing its structure. Ω_{IBM} boundary is delimited with a black rectangle. The blue rectangle delimits the core-region, it is the smaller cylinder that encloses the RBC (aligned with $\overrightarrow{u_{\text{RBC}}}$). The core region is built around an RBC whose centroid is designated by a black circle and the membrane grid nodes are depicted with a black square.

4. The remeshing metric is assigned to all vertices of the existing grid, based on whether their associated elements lie within the new fine region. For all grid nodes located in the overlapping area between the previous and the new fine region, the mesh is frozen to avoid modification.
5. The metric field over the entire fluid grid is iteratively modified so that $\nabla h(\vec{x}) < \nabla h_{\max}$.
6. The MMG3D library is called to perform remeshing, and the solution from the old grid is interpolated onto the new one. The next iteration proceeds.

In section 3.1, results obtained with and without MA are compared, and the computational cost savings are evaluated as a function of the remeshing algorithm's free parameters, l_{ext} and r_{ext}.

2.1.3 | Numerical pipeline: from the input parameters to the resistive pulse

Simulations without RBCs

From the industrial geometry shown in Fig. 1a, the fluid domain is defined. It includes the RBC tank, the micro-orifice and the exit tube. A constant flow rate of 7.74×10^{-9} m^3.s^{-1} is imposed at the inlet to replicate the pressure differential applied in the ABX Micros 60. The electrolyte classically used in the ABX Micros 60 is mainly composed of water. Therefore, we set $\nu_{ext} = 1.0 \times 10^{-6}$ m^2.s^{-1} and $\rho = 1000$ kg.m^{-3}. In addition, the electric potential without cell is computed to assess the resistance of the system in the absence of RBC, R_{CF}. The conductivity of the electrolyte is set to $\sigma_{ext} = 2.27$ S.m^{-1}. A potential of U =13.9 V is applied between the electrodes, as in the ABX Micros 60. Other walls are assumed to be insulating.

To compute the carrying flow in the cell-free configuration, the grid is set with a mesh size of 1.6 µm in the micro-orifice region, while the mesh size gradually increased with a growth rate of 1.3 in the rest of the configuration, so that mesh size in the coarser region of the domain reach 500 µm. The total number of elements is approximately 3.0×10^7.

Deformation of the RBC in the tank before reaching the orifice (FSI, phase I)

The output of interest of the CC simulations is the pulse associated with the passage of an RBC in the micro-orifice, which depends on the RBC deformation in the orifice itself. However, in the industrial CCs, RBCs can be deformed by the flow upstream of the orifice. Neglecting this deformation leads to erroneous predictions in the orifice [19]. As a full-scale simulation of the RBC

dynamics within the entire device would be computationally expensive and impractical, the RBC deformation by the flow before the orifice is predicted in a first FSI simulation, referred to as phase I. This approch has been validated by Taraconat *et al.*[19].

Instead of predicting the RBC deformation in the full system, it is calculated in a small domain, by applying the same strain-rate tensor history as in the real system. In this phase I calculation, the RBC is fixed, aligned with the strain direction, and subjected to a pure elongational flow representative of the conditions experienced upstream of the aperture. Velocity gradients are extracted along a streamline — taken as a good approximation of the RBC trajectory — from the cell-free simulation, and imposed as time-dependent Dirichlet boundary conditions on a cylindrical domain. This is illustrated in Figure 4a, in which the streamlines are characteristic of a purely linear extensional flow, in the frame of the RBC. For the FSI calculations, the IBM requires that the fluid grid resolution be comparable to the solid grid size h_{RBC}[26]. In Phase I simulation, the RBC's center of mass remains approximately centered within the domain. Accordingly, a mesh size of $h_{\mathrm{RBC}} = 0.3$ µm was applied within a spherical region of radius = $\sqrt{\frac{S_{\mathrm{RBC}}}{\pi}}$ (twice the length of the longest axis of the RBC at rest) centered at the domain centroid. Outside this region, the mesh size was set to 1.0 µm, resulting in a total of approximately 6×10^5 elements.

While the time-history of the velocity gradient only depends on the trajectory, which is fixed in this study, this calculation has to be performed for each set of RBC parameters. The resulting RBC state serves as the starting configuration for the RBC in phase II.

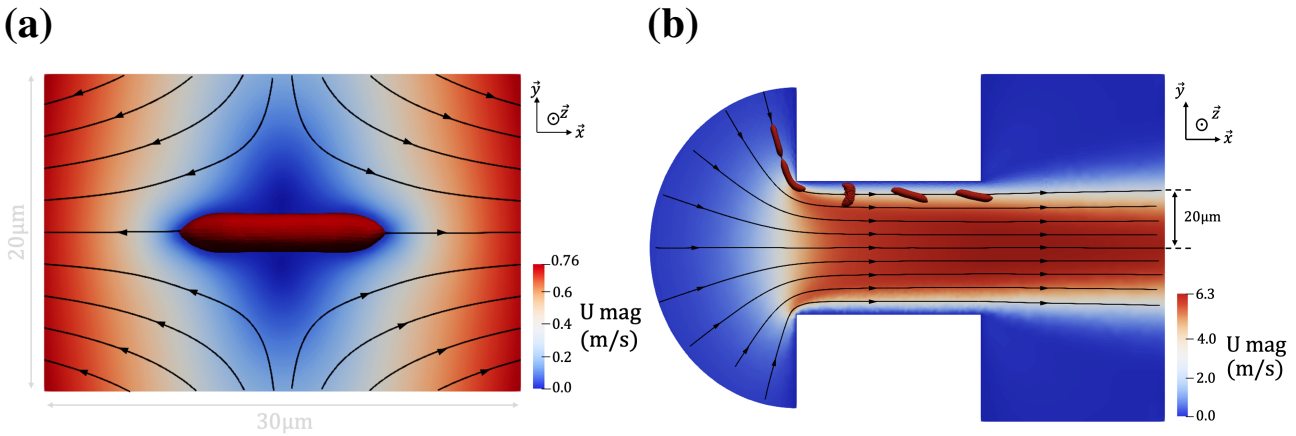

FIGURE 4 The two phases FSI calculation. (a) Phase I: Slice of the domain in which the deformation of the RBC upstream of the micro-orifice is mimicked by applying the correct strain-rate tensor along time. The colormap shows the fluid velocity magnitude. The flow is extensional and is outlined with black streamlines. The boundary conditions are deduced from the strain-rate tensor experienced by an RBC from the bulk of the tank until ≈ 10 µs before it would enter the orifice. (b) Phase II: Slice of a small portion of the domain around the orifice. The colormap represents the fluid velocity magnitude in the absence of RBC. Streamlines are outlined in black. An example of RBC dynamics near the orifice wall is superimposed by displaying the shape of the membrane at five instants. The initial RBC state for that calculation (phase II) is the last RBC state of the calculation presented Figure 4a (phase I).

Deformation of the RBC in the orifice (FSI, phase II)

Phase II focuses on the RBC dynamics within the orifice, with the computation restricted to a portion of the industrial geometry surrounding the orifice (see Figure 4b). The constant flow rate in the entire device also passes through the orifice. It is imposed at the inlet of the domain (left of Figure 4b). The RBC is deposited before the orifice in its deformed state after Phase I calculation. In the orifice, the trajectory is such that the RBC flows at 5 microns from the wall and 20 microns from the orifice axis.

In the FSI Phase II domain, elements of size h_{RBC} are restricted to a limited zone around the cell, using dynamics mesh adaptation as described in section 2.1.2. Outside this refined region, the mesh size was set to 1.0 µm in the orifice area, while the mesh size gradually increased with a growth rate of 1.3 in the rest of the configuration, so that mesh in the coarsest region of the domain reaches 5 µm. The total number of elements for this configuration is approximately 1.3×10^7.

Impedance pulse

The impedance pulse is obtained by computing a series of electrostatic problems to determine the additional resistance of the system due to the RBC. An accurate description of a pulse is achieved by computing this resistance every microsecond. Results from phase II FSI simulations are thus stored every microsecond and used as an input of the electrostatic calculations. The same boundary conditions as in the electrostatic cell-free simulation are applied. However, the mesh used here differs due to the presence of an RBC, which requires finer elements of size h_{RBC} in the region occupied by the RBCs.

Computing resources, and calculation cost

Each simulation was conducted on one node with 128 cores. Each compute node is equipped with dual AMD EPYC 7xx2 series processors, running at 2.6 GHz and 256 GB of RAM. Using the dynamics remeshing for phase II, calculations in phase I, phase II and the series of electrostatic calculations take approximately the same CPU time. The total computational cost was approximately 600 CPU hours for one pulse, corresponding to slightly less than 5 hours of wall-clock time.

2.2 | Experimental set-up

2.2.1 | Sample and instrument

This study uses nine human healthy blood samples collected during routine medical care and provided anonymously to HORIBA in compliance with ethical and regulatory standards. The blood samples were analyzed, less than 6 hours after collection, using the ABX Micros 60 from HORIBA. It features an enhanced bandwidth of 150 kHz to minimize signal distortion caused by the electronics in the standard commercial model[19,25]. Upon insertion of the sample tube, a needle withdraws an aliquot and transfers it to the RBC tank. The sample is then diluted 1/15000 in a phosphate buffered saline (PBS) electrolytic reagent, formulated with an osmolarity of 297 mOsm. A vacuum pump then aspirates the suspension through a micro-orifice with a 200 mbar pressure drop across the aperture. The geometry of the RBC tank and of the micro-orifice are sketched in Figures 1a-1b.

During vacuuming, a constant electric current is applied using the two electrodes. Note that the electric conditions applied differ from the standard experimental setup of the ABX Micros 60 (described in Taraconat *et al.*[25]). Indeed, a PBS reagent has been used as it is presumed not to alter RBCs properties, but its conductivity (approximately 2.7 $\mathrm{S.m^{-1}}$ at 35°) is about 1.2 times greater than the standard reagent. Moreover, there were concerns about electroporation effects at the typical electric current level[56]. As a result, the electric current was reduced by a factor of 1.3, resulting in a steady current of 0.41 mA, which was chosen to maintain an optimal signal-to-noise ratio.

Pulses are recorded thanks to an in-house Lab-VIEW^{TM} (National Instruments) code[19]. During the recording, the raw experimental signatures undergo modifications by the ABX Micros 60 hardware: amplified for ensuring their usability in the rest of the system and then edited with a bandpass filter to minimize the noise.

2.2.2 | Pulse selection for comparison

As stated in section 2.1.1, the study focuses on a single trajectory. Ideally, the numerical results should be compared to experimental pulses for the same trajectory. However, it is impossible to directly determine the trajectory associated to a pulse in the experiments. However, we can select experimental pulses that share some specific features with the simulations, which are strongly correlated with the trajectory. As demonstrated in the work of Taraconat *et al.*[19],the RBC trajectory influences the pulse width and the time at which the rotation-peak is generated: when the RBC flows closer to the orifice wall, its velocity decreases, resulting in a longer pulse duration; in addition, the shear rate (here the gradient of axial velocity with respect to the direction normal to the wall) is higher, causing the RBC to rotate earlier. Two pulse characteristics, measuring the pulse duration and the rotation-peak period, are therefore used for pulse selection, and defined in Figure 5a.

W_T is the width of the pulse above a threshold T: it is the time during which $\Delta R \geq T$. W_T informs about the time taken by an RBC to flow through the micro-orifice. P_T is the rotation-peak relative position, calculated as: $P_T = \frac{W_P}{W_T}$, with W_P the time delay between the moment when the signal exceeds the threshold T (t = t_T) and the moment when the signal reaches its maximum ΔR_{max}, which generally corresponds to the rotation peak. Note that T is set to 50% of ΔR_{max}[25]. P_T characterizes the moment when the cell rotates in the micro-orifice. The smaller P_T, the earlier the rotation. Since they are partly controlled by the RBC trajectory, these two metrics are used in section 3.3 for filtering experimental signature by trajectory. To filter the experimental pulses, the minimum and maximum values of W_T and P_T were assessed across all simulated signatures, and any pulses outside

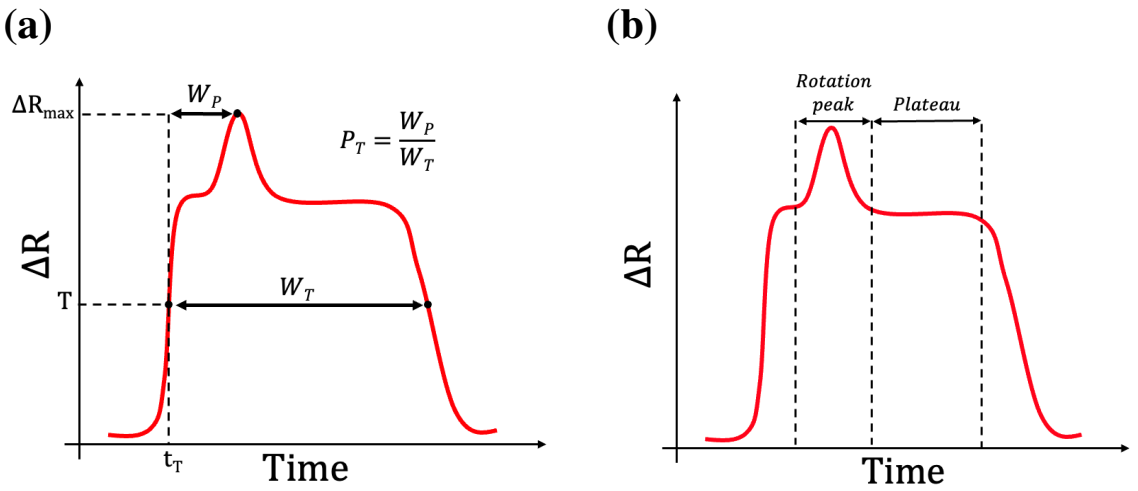

FIGURE 5 Characterization of impedance pulses. The red curves represent schematic impedance signatures. (a) Illustration of signatures characteristics W_T and P_T introduced for filtering experimental signatures by trajectory. (b) Delimitation of signature zones of interest for inspecting the effect of RBC deformability.

these established limits were discarded. Obviously, this technique is an approximation of a trajectory selection. From previous results, we estimate that the uncertainty in the radial position of RBC passage is below 5% of the aperture radius.

Hardware modifications applied to experimental pulses (c.f. section 2.2.1) are not modeled in the simulations. Indeed, the gain applied to experimental pulses adjusts to compensate for the effects induced by temperature variation and has not been measured during data acquisition. Direct comparison between simulated and experimental results is therefore impossible. To overcome this issue, both numerical and experimental pulses are expressed in terms of resistive perturbation, then normalized with a pulse-dependent scaling factor. This factor is equal to the "plateau" amplitude illustrated in Figure 5b. As previously stated, the main effects of deformability on pulses are expected in the rotation peak region. Therefore, scaling pulses by the plateau amplitude emphasizes the effects of RBC deformability on pulses. The plateau amplitude is computed at time $t = t_T + 0.70W_T$, as this is a moment when the pulse's slope from simulated data (presented in sections 3.2 - 3.3) is the closest to zero on average. The notation ΔR^* denotes the scaled amplitude of the numerical pulses. This normalization strategy also mitigates the influence of RBC volume on the pulse signals, thereby emphasizing the other RBC properties[25].

3 | RESULTS

3.1 | Numerical approach validation and optimization

In this section, the reliability of the numerical approach and the efficiency of the mesh adaptation strategy are assessed. First, a simulation was performed using a static fluid grid, which serves as a reference: instead of using dynamic remeshing, the fluid grid is refined all along the trajectory to ensure good accuracy of the IBM without needing to remesh. This correspond to the previous state of the art in CC simulations[19,25]. Subsequently, multiple simulations were conducted to assess the impact of the user-defined parameters (l_{ext} and r_{ext}) that control the size of the refinement region in the dynamic remeshing. Nine simulations with MA were performed, combining three values for both r_{ext} and l_{ext}: 1 µm, 5 µm, and 10 µm.

The RBC parameters used in this study are: $G_s = 2.5$ µN.m^{-1}, $E_a = 2.5 \times 10^{-1}$ N.m^{-1}, $E_b = 6.0 \times 10^{-19}$ J, $Q = 0.65$, $\nu_{in} = 18.0 \times 10^{-6}$ m^2.s^{-1}, $\eta_{memb} = 0$ and $\phi = 0$. Figure 6a and Figure 6b illustrate simulation results obtained at different time instants using a static fluid grid and a dynamically adapted grid with $l_{ext} = 5$ µm and $r_{ext} = 1$ µm, respectively. Figure 6c presents examples of grids generated during the initialization for various sets of l_{ext} and r_{ext}.

The resulting RBC dynamics (not shown here) are very similar across all cases. Before entering the orifice, the RBC undergoes significant elongation and maintains this elongated shape throughout its passage. It rotates during the first third of the orifice, then gradually realigns with the aperture axis before exiting.

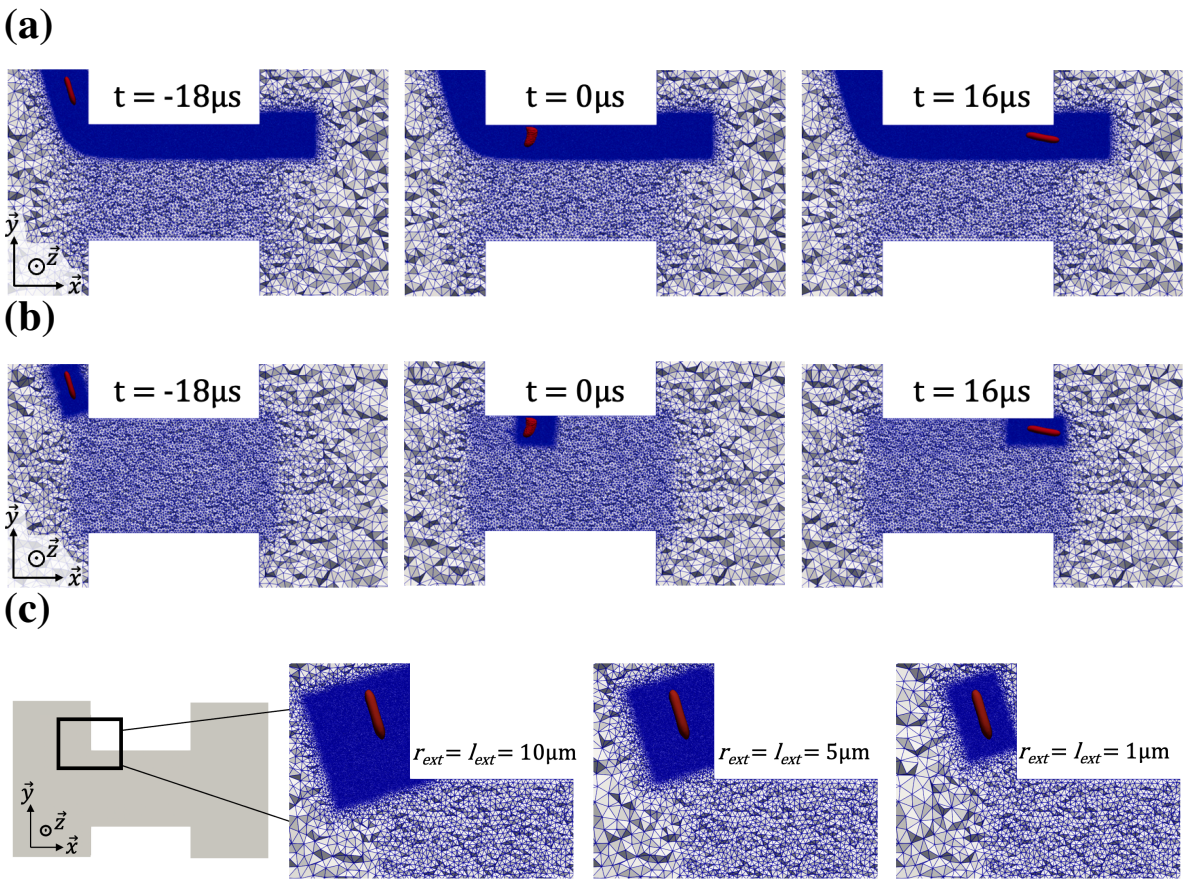

FIGURE 6 Simulations of the FSI calculation phase II, with and without MA. (a) RBC states and fluid grids at different instants in a simulation performed with a static fluid grid. The times reported are shifted so that t=0 when the RBC is rotating and the associated pulses reaches its maximum amplitude. At t=−18 µs, the RBC is too far from the aperture entrance and the electric perturbation of the RBC is negligible. At t=16 µs, the RBC is exiting the aperture and the resisitive perturbation decreases (descending slope after plateau region). (b) RBC states and fluid grid states at different instants in a simulation with MA (l_{ext} = 5 µm, r_{ext} = 1 µm). (c) Examples of MA cases performed with different Ω_{IBM} size, focusing on the upper area at the orifice entrance. The grids are obtained at initialization (t=-18 µs) of FSI phase II calculation.

Figure 7 shows the corresponding resistance pulses. All cases performed with MA are represented by a green envelope indicating the minimum and maximum ΔR values at each time instant. The result for the case without MA is represented by a solid black line. Additionally, results obtained by Taraconat *et al.*[25] under identical conditions (same RBC, trajectory, flow parameters, and geometry), but using a different static grid, are also plotted for comparison. The green envelope closely follows the black solid line, indicating that the MA strategy yields results nearly identical to those obtained with a static grid. Furthermore, the strong agreement with numerical results from Taraconat *et al.*[25] (previously validated against experimental data) supports the reliability of our numerical approach. The deviation in ΔR is always less than 4%, confirming the accuracy of the simulations. MA was tested on other trajectories, with similar accuracy.

The performances are now assessed. Figure 8a shows the computational cost of each MA case, normalized by the cost of the simulation performed with the static fluid grid. For all tested combinations of l_{ext} and r_{ext}, the cost ratio is less than 1, indicating that the reduction in the number of elements achieved thanks to MA effectively lowers the computational cost during the FSI phase II calculation despite the additional cost of remeshing. For reference, the grid shown in Figure 6a (without MA) contains approximately 13×10^6 elements, whereas the dynamically adapted grid in Figure 6b averages around 2×10^6 elements.

As shown in Figure 8a, the observed cost reductions are primarily driven by variations in r_{ext}, as expected. The volume of the refined region is indeed proportional to $(r_c + r_{ext})^2(l_c + l_{ext})$, so changes in the radial dimension naturally have a larger impact.

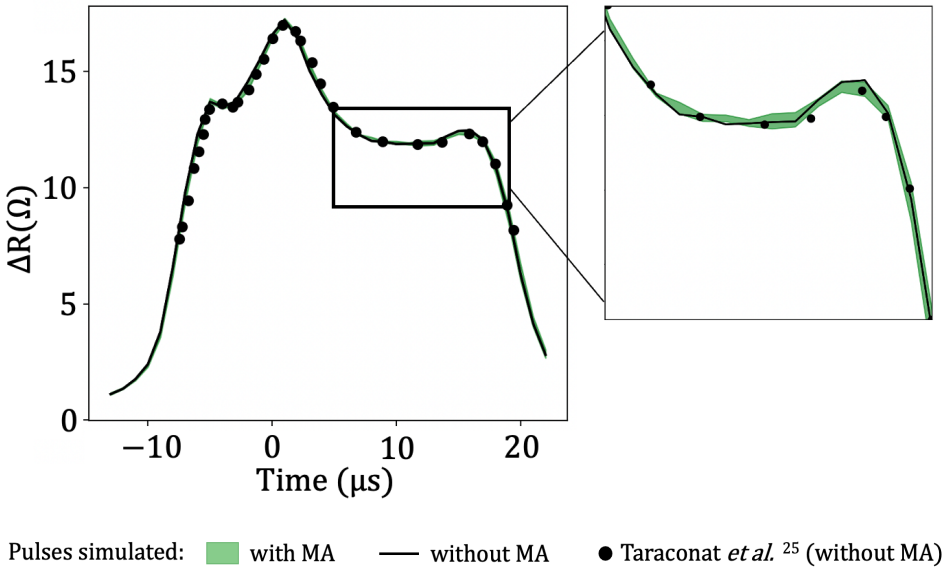

FIGURE 7 Impedance signatures resulting from simulations with and without mesh adaptation. The pulses obtained with MA are enclosed in a green envelope indicating the minimum and maximum values of ΔR at each time instant, over all cases. The pulse obtained using a static fluid grid is shown as a solid black line. Black dots represent a reference pulse previously obtained under the same conditions with a static grid, as reported in Taraconat *et al.* [25].

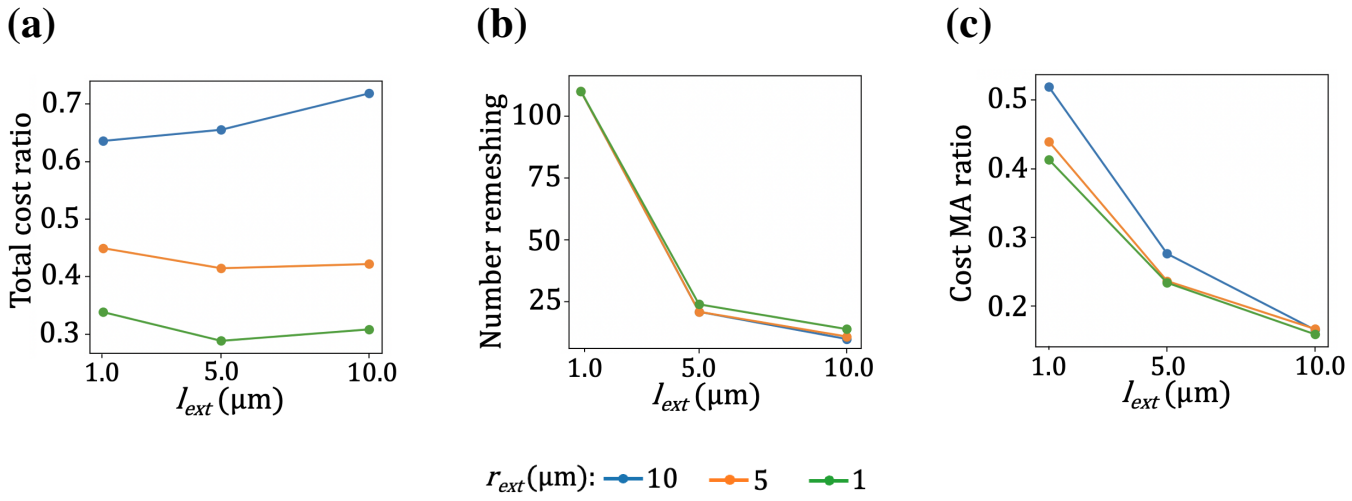

FIGURE 8 Performance metrics of the simulations using mesh adaptation during FSI calculation phase II. The results are plotted as a function of l_{ext} and correspond to different configurations of the fine region around the RBC. Curve colors correspond to different values of r_{ext}. (a) Cost of each MA case, normalized by the cost of a simulation without MA. (b) Number of remeshing events triggered during the simulation. (c) Proportion of total computational cost attributed to the mesh adaptation process.

Furthermore, the RBC geometry yields a core region around the cell such that $r_c < l_c$, so variations in the radial extent relatively influence the refined volume more significantly than changes in length. Interestingly, the number of remeshing operations per simulation, shown in Figure 8b, is largely governed by l_{ext}: the greater the value of l_{ext}, the fewer remeshing operations are required. This behavior is relatively insensitive to r_{ext}, which suggests that the optimal global performance is achieved for small values of r_{ext}. Figure 8c further indicates that, in addition to increasing the volume of the fine region, large values of r_{ext} also raise

the computational cost associated with remeshing. Finally, according to Figure 8a, an optimal value of l_{ext} appears to be around 5 µm when $r_{ext} < 10$ µm. This value provides a good compromise between remeshing frequency and overall simulation cost.

Among all configurations tested, the fastest simulation corresponds to $r_{ext} = 1$ µm and $l_{ext} = 5$ µm. While the original approach using a static fluid grid requires 732 hours (CPUh) for this phase II calculation, the most efficient MA configuration completes the simulation in 211 CPUh. Consequently, mesh adaptation with $r_{ext} = 1$ µm and $l_{ext} = 5$ µm was used for the studies presented in sections 3.2 and 3.3. Accounting for the whole series of calculations, mesh adaptation for phase II reduces the total cost of simulating a pulse by approximately a factor of two.

3.2 | Influence of RBCs properties on pulses

In this section, the effect of RBC orientation, shape, and mechanical properties on resistance pulses is assessed using a one-at-a-time (OAT) approach. From several reference parameter sets, individual parameters (G_s, ν_{in}, Q, ϕ and η_{memb}) are increased, allowing their influence on the pulses to be isolated.

The OAT analysis was first conducted using a reference case in which all parameters were set to their lower bounds, except for Q and η_{memb}, which were fixed at intermediate values due to numerical instabilities at lower levels (see Section 3.3). From this reference case, the analysis was repeated with five alternative reference cases to test the robustness of the conclusions: in each, all parameters remained at their baseline values except one, which was increased to its maximum physiological value. The exact parameter values for all the reference cases and the sensivity analysis runs are listed in Table 2. Figures 9a-9f present the resistance pulses from the sensitivity analysis. The time axis is shifted such that $t = 0$ corresponds to the pulse's rotation peak, and the pulses are normalized (see section 2.2.2) to eliminate the influence of RBC volume, which depends on Q.

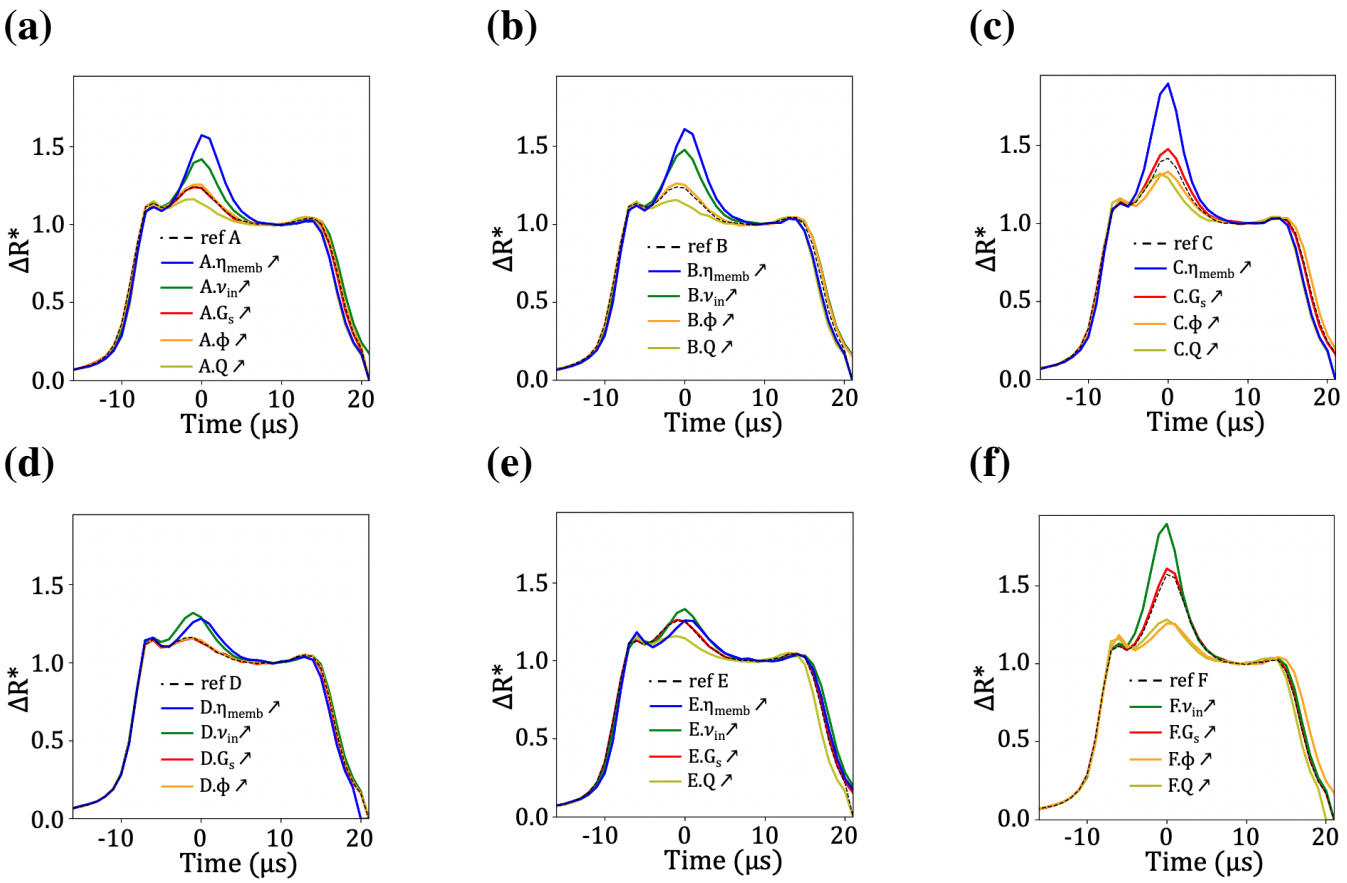

FIGURE 9 One-at-a-time sensitivity analysis of the numerical pulses when varying RBC properties (η_{memb}, ν_{in}, G_s, ϕ and Q). Six different operating cases were used (see the different scenarios in Table 2).

TABLE 2 Overview of the cases used to study the sensitivity of pulses to different RBC properties. Each block between two horizontal lines represents a one-at-a-time study conducted at a specific operating point, labeled as "ref" followed by a letter (A, B, C, D, E, or F). Relative to the operating point, individual parameters (G_s, ν_{in}, Q, ϕ, and η_{memb}) are increased, and each resulting case is labeled with the same letter as the associated reference point, the modified parameter, and the symbol "↗". For each case, the value of each parameter is provided, with the increased parameter highlighted in bold. The values E_a = 0.25 N·m^{-1} and $E_b = 6.0 \times 10^{-19}$ J are used in all calculations.

Case	G_s (μN.m^{-1})	ν_{in} (10^{-6}m^2.s^{-1})	Q	ϕ	η_{memb} (10^{-9} Pa.m.s)
ref A	2.2	7.0	0.68	0	5.0
A.G_s ↗	**22.5**	7.0	0.68	0	5.0
A.ν_{in} ↗	2.2	**15.0**	0.68	0	5.0
A.Q ↗	2.2	7.0	**0.78**	0	5.0
A.ϕ ↗	2.2	7.0	0.68	$\frac{\pi}{2}$	5.0
A.η_{memb} ↗	2.2	7.0	0.68	0	**25.0**
ref B	22.5	7.0	0.68	0	5.0
B.ν_{in} ↗	22.5	**15.0**	0.68	0	5.0
B.Q ↗	22.5	7.0	**0.78**	0	5.0
B.ϕ ↗	22.5	7.0	0.68	$\frac{\pi}{2}$	5.0
B.η_{memb} ↗	22.5	7.0	0.68	0	**25.0**
ref C	2.2	15.0	0.68	0	5.0
C.G_s ↗	**22.5**	15.0	0.68	0	5.0
C.Q ↗	2.2	15.0	**0.78**	0	5.0
C.ϕ ↗	2.2	15.0	0.68	$\frac{\pi}{2}$	5.0
C.η_{memb} ↗	2.2	15.0	0.68	0	**25.0**
ref D	2.2	7.0	0.78	0	5.0
D.G_s ↗	**22.5**	7.0	0.78	0	5.0
D.ν_{in} ↗	2.2	**15.0**	0.78	0	5.0
D.ϕ ↗	2.2	7.0	0.78	$\frac{\pi}{2}$	5.0
D.η_{memb} ↗	2.2	7.0	0.78	0	**25.0**
ref E	2.2	7.0	0.68	$\frac{\pi}{2}$	5.0
E.G_s ↗	**22.5**	7.0	0.68	$\frac{\pi}{2}$	5.0
E.ν_{in} ↗	2.2	**15.0**	0.68	$\frac{\pi}{2}$	5.0
E.Q ↗	2.2	7.0	**0.78**	$\frac{\pi}{2}$	5.0
E.η_{memb} ↗	2.2	7.0	0.68	$\frac{\pi}{2}$	**25.0**
ref F	2.2	7.0	0.68	0	25.0
F.G_s ↗	**22.5**	7.0	0.68	0	25.0
F.ν_{in} ↗	2.2	**15.0**	0.68	0	25.0
F.Q ↗	2.2	7.0	**0.78**	0	25.0
F.ϕ ↗	2.2	7.0	0.68	$\frac{\pi}{2}$	25.0

In general, the influence of the parameters is essentially the same regardless of the chosen reference scenario. Specifically, increasing Q (yellow lines) leads to flatter pulses, whereas increasing ν_{in} (green lines) or η_{memb} (blue lines) produces pulses with sharper, more pronounced rotation peaks relative to the reference cases (black dash lines). In the scenario where all simulations were conducted with increased sphericity (Figure 9d), these trends remain valid; however, the effect of RBC rigidity is less pronounced compared to the low-sphericity cases. In constrast, increasing G_s results in no significant changes compared to the reference responses, indicating that variations in shear modulus within physiological limits have a negligible effect on the pulses. This is further supported by the similarity between Figures 9a and 9b, where the pulses remain essentially unchanged despite a tenfold increase in G_s.

Finally, Figures 9c and 9f show that the influence of the initial orientation ϕ (orange lines) depends on RBC rigidity, whether controlled by internal viscosity ν_{in} or membrane viscosity η_{memb}. In the scenarios where the reference case has $\nu_{in} = 7 \times 10^{-6}$ m^2.s^{-1} and $\eta_{memb} = 5 \times 10^{-9}$ Pa.m.s, varying ϕ has little to no effect. In contrast, when $\nu_{in} = 15 \times 10^{-6}$ m^2.s^{-1} or $\eta_{memb} = 2.5 \times 10^{-8}$ Pa.m.s, ϕ significantly alters the pulse shape. In particular, changing ϕ from 0 to $\frac{\pi}{2}$ produces a pulse with a more subdued rotation peak. This result is illustrated in Figure 9e, where pulses simulated with $\frac{\pi}{2}$, exhibit reduced variability compared to the corresponding $\phi = 0$ cases shown in Figure 9a.

Overall, increasing RBC rigidity extends the range of possible rotation peak amplitudes, either preserving or enhancing the peak height depending on the parameter combination. Conversely, increasing RBC sphericity tends to reduce pulse variability in the rotation-peak region.

3.3 | Comparison with experimental data

In this section, the model's ability to reproduce the range of signatures observed experimentally is assessed (particularly in the rotation peak region). To this end, a systematic numerical parametric study was conducted involving five parameters: G_s, ν_{in}, Q, ϕ, and η_{memb}. For each parameter, three levels were defined to explore the ranges of values reported for healthy RBCs (see Table 1). All possible combinations of these parameter levels were simulated, resulting in $3^5 = 243$ simulations. Although the earlier one-at-a-time analysis showed that G_s had a limited effect on the pulse shape, it was retained in this study to ensure comprehensive coverage of physiologically relevant conditions. Numerical instabilities occurred in 8 of the 243 cases (approximately 3%). These unstable cases were consistently associated with $Q = 0.57$ and $\eta_{memb} = 0$, further supporting the importance of incorporating membrane viscosity into the modeling framework.

Next, data acquisition was performed on nine healthy subjects using the ABX Micros 60 analyzer, as described in section 2.2. Approximately 15000 pulses were recorded per acquisition. For the sake of clarity, results are shown for a single representative sample; similar results were obtained for other samples. For each of the experimental (red dots) and simulated (green dots) pulses, the metrics W_T and P_T are computed (Figure 5a), and the values are displayed in Figure 10. The simulated results are clustered within a confined region of the (W_T, P_T) space, where the experimental data are densely concentrated. A black rectangle indicates the filtering window applied to retain experimental pulses likely associated with RBCs following a trajectory similar to the one fixed in the simulations (see section 2.2). Note that W_T and P_T results are modulated by the RBC properties and initial orientation ϕ, which explains the variability observed in Figure 10, even when simulations are conducted along a single trajectory.

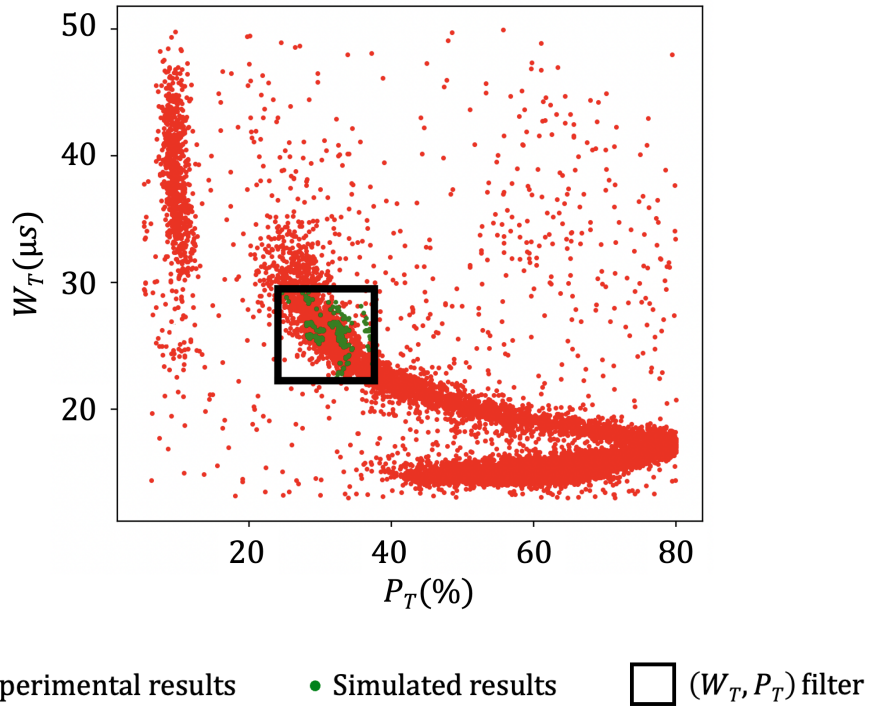

FIGURE 10 Scatter plot of experimental (red dots) and numerical (green dots) results in the (W_T, P_T) plane. The black rectangle delineates the filtering criterion used to extract experimental pulses corresponding to RBCs that followed trajectories similar to the one imposed in the simulations.

The filtered experimental signatures and the simulated signatures are presented in Figures 11a - 11d, with green and red solid lines, respectively. Simulation results are presented by grouping the results by the value of η_{memb} imposed. Given the large number of experimental pulses recovered, a median experimental pulse was computed to highlight the general trend, and shown in Figures 11a - 11d as a black curve.

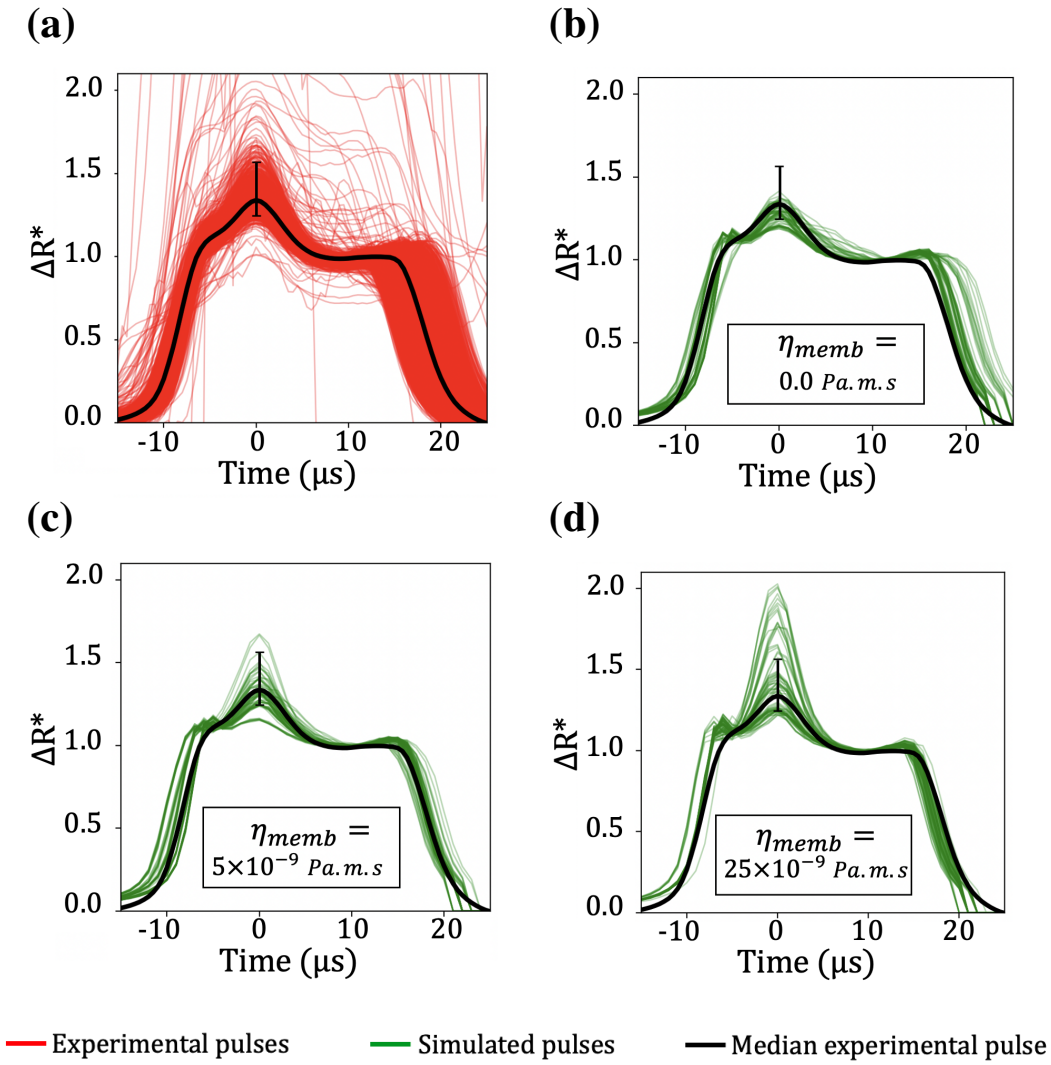

FIGURE 11 Comparison between experimental and simulated normalized pulses. All pulses are shifted in time so that their peak amplitude occurs at $t = 0$. Simulated signatures (green lines) result from a systematic parametric study. Panels (b), (c), and (d) show simulated pulses generated with η_{memb} values of 0, 5×10^{-9} Pa.m.s, and 2.5×10^{-8} Pa.m.s, respectively. Panel (a) displays experimental pulses (red lines) obtained using the ABX Micros 60 on a healthy subject. The filtered experimental pulses correspond to RBCs following trajectories similar to those used in the simulations. The solid black curve represents the median experimental pulse. The vertical black segment marks the rotation peak amplitude range of the experimental signatures, defined by the 5th to 95th percentiles.

The simulations closely reproduce the experimental signatures, particularly for the subset of results in which $\eta_{memb} = 5 \times 10^{-9}$ Pa.m.s. Figures 11b - 11d show that increasing η_{memb} leads to a broader range of simulated pulse shapes in the rotation peak region. This observation is consistent with the findings reported in section 3.2. Note also that the experimental pulses appear smoother, with a steady rise toward the peak, while simulated pulses present an initial secondary peak just before the main rotation peak. Possible explanations are discussed in section 4.

The amplitude range of experimental pulses at $t = 0$ is represented by a vertical black segment in Figures 11b - 11a. This segment indicates the rotation peak amplitude between the 5th and 95th percentiles of the experimental data. When membrane viscosity is neglected ($\eta_{memb} = 0$), the simulated pulses do not fully span the range defined by this segment. Conversely, when $\eta_{memb} = 2.5 \times 10^{-8}$ Pa.m.s, almost 50% of the simulated pulses fall outside this range. Among the cases tested, $\eta_{memb} = 5 \times 10^{-9}$ Pa.m.s provides the best agreement with the experimental data, suggesting it is the most physiologically consistent value for healthy RBCs, in this configuration.

4 | DISCUSSION

This study presents a numerical approach for simulating Coulter-based systems, capable of predicting both red blood cell (RBC) dynamics and the associated electric resistance signals. The numerical framework is built upon the method of Taraconat *et al.*[19], solving first the fluid–structure interaction problem (without RBC damage) and subsequently the electric problem, while neglecting coupling effects of the electric field on cell deformation. Regarding the numerical efficiency, the proposed framework incorporates a dynamic mesh adaptation (MA) strategy that enhances simulation flexibility while significantly reducing computational costs. Compared to the original method using a static fluid grid[19], the implementation of MA reduces the computational cost of the FSI calculation in the orifice region, resulting in an overall cost reduction of approximately 50% per pulse. Although the computational gain is already substantial, further improvements may be possible by fine-tuning the shape of the refined region. For example, employing an ellipsoidal configuration can minimize the radial extent of the fine mesh region. In any case, the reduction in computational cost enables the execution of an extensive simulation campaign involving the systematic variation of RBC properties across a five-dimensional parameter space. As a guideline, the simulation plan required approximately 140,000 CPU hours, corresponding roughly to 20 nodes with 128 cores operating over 2 days. While the computational cost is non-negligible, it remains well within reach using high-performance computing resources.

The high CPU cost of the simulations can be explained by the number of simulations to perform, but also the extreme conditions involved, including high extensional and shear stresses, high Reynolds numbers (a few hundreds in the orifice), as well as by the separation of time scales in the problem. For instance, the extension of the particles prior to their passage through the orifice is simulated over a duration of half a second while the time step is 6 orders of magnitude smaller. The YALESB2IO code uses an explicit time advancement scheme, which is constrained by time-step stability and accuracy requirements. Although alternative methods could potentially be faster, the lack of similar applications in the literature makes it difficult to predict their possible efficiency.

The pulses exhibit a plateau, used here for non-dimensionalizing the signals, corresponding to a period during which the RBCs flow steadily with minimal changes in deformation and orientation. This plateau is typically preceded by a rotation-peak. The amplitude difference between the peak and the plateau serves as an indicator of the RBC shape anisotropy during rotation. This difference is sensitive to the mechanical properties of the RBC and can vary significantly from one pulse to another.

A total of five RBC parameters were investigated numerically: membrane shear modulus (G_s), cytoplasm viscosity (ν_{in}), RBC volume ratio (Q), membrane viscosity (η_{memb}), and initial RBC orientation (ϕ). Except for G_s, pulse sensitivity was observed for each of these parameters across ranges corresponding to healthy RBCs. To the best of our knowledge, the effects of RBC membrane viscosity (η_{memb}) and initial orientation (ϕ) have not been previously investigated in this context. Our results show that both parameters significantly influence the pulse characteristics.

The loading time experienced by the RBCs in the orifice is short enough to allow variations in membrane viscosity and cytoplasmic viscosity to influence the RBC dynamics, even for η_{memb} values lower than those reported in the literature for healthy RBCs. When RBC viscosity increases, the amplitude of the rotation-peak tends to rise. This effect may be attributed to changes in the shape factor induced by increased viscosity: higher viscosity results in reduced RBC deformability. Conversely, increasing RBC sphericity leads to a reduction in the observed rotation peak, as more spherical particles exhibit less visible rotation. Consequently, a more attenuated rotation peak is expected with increasing sphericity (as reflected in Q). These tendencies corroborate previous experimental results[25] which showed that rotation peak amplitude increases when the RBC is stiffened, and decreases when the RBC is spherized.

Regarding RBC initial orientation, ϕ effects are only detected for the RBCs with the highest rigidity level. Upstream of the orifice, the extensional flow tends to stretch deformable RBCs into an elongated shape aligned with the flow direction. These shapes are approximately axisymmetric around the flow direction, so ϕ, which measures the orientation around this axis, naturally has no significant effect on the resulting dynamics and the associated pulse. However, more rigid RBCs (e.g., for $\nu_{in} = 15 \times 10^{-6}$ m^2.s^{-1} or $\eta_{memb} = 2.5 \times 10{-}8$ Pa.m.s) retain a shape closer to their equilibrium discocyte shape. Moreover, the

upstream flow does not alter the initial RBC orientation ϕ (c.f. section 2.1.1), so this initial orientation is preserved. In such cases, ϕ has a significant effect, as it determines how the cell's geometry is aligned with respect to the shear stress encountered in the orifice. As suggested by Grover *et al.*[50], a rigid oblate particle entering the boundary layer of the orifice with an orientation $\phi = \frac{\pi}{2}$, undergoes a rolling motion around its minor axis and maintains a constant shape factor. In contrast, an initial orientation $\phi = 0$ leads to tumbling motion, resulting in a time-varying shape factor. As a result, the influence of ϕ is expected to increase with RBC stiffness, with the rotation peak showing a decreasing trend as ϕ shifts from 0 to $\frac{\pi}{2}$. It is important to emphasize that the effects of ϕ and RBC rigidity, as discussed above, are significantly influenced by RBC morphology and may be different in patho-physiological condition. For example, in spherocytosis - where RBCs become more spherical - the effects of ϕ may vanish, even at high rigidity levels. In sickle cell disease - where cells adopt a characteristic sickle shape - the effects of ϕ may become apparent even at lower rigidity thresholds.

Thereafter, all results from the systematic numerical parametric study were used to evaluate the model's capacity to reproduce the diversity of pulses observed in experiments, for RBCs traveling near the orifice wall. The numerically generated pulses were qualitatively compared with experimental data acquired from a healthy blood sample analyzed using the ABX Micros 60 analyzer.

The overall shape of the pulses predicted by the simulation tool aligns well with the experimental measurements. However, systematic discrepancies are observed at the beginning of the pulses, where the simulations exhibit a secondary peak preceding the rotation peak. This effect is also observed, albeit less pronounced, at the end of the pulse plateau. Several hypotheses can be made to explain this discrepancy. First, the impact of the electric field on the RBC dynamics was not considered. However it is known that electric effects may modulate the RBC shape within the observed electric field range imposed[57,58]. Accounting for the electric effects[59] should further improve the quality of the predictions. Second, the electric field predicted in the simulations may differ from that in the experiment, particularly near the orifice corners. In the simulations, these corners are modeled as sharp angles, whereas in reality, fabrication imperfections prevent such ideal geometries. As a result, the electric field may be overestimated at the entrance and exit of the orifice in the numerical model, which is indeed consistent with the secondary peaks present in the simulation pulses. Finally, it should be noted that the raw experimental signals are subjected to filtering to reduce measurement noise (see section 2.2.2), which is expected to further smooth the signals and magnify the difference with simulated pulses.

Subsequently, we assessed the experimental variability in rotation-peak amplitude and aligned it with simulation results to empirically estimate membrane viscosity. In simulations that neglect membrane viscosity, the observed experimental variation in the rotation-peak is not fully captured. This indicates that membrane viscosity plays a critical role. Considering that reported values of RBC membrane viscosity in the literature span several orders of magnitude, various viscosity values were tested in the simulations and compared against experimental data. In the specific modeling framework used in this paper, the membrane viscosity that yields the closest agreement between the simulated and experimental pulses is $\eta_{memb} = 5 \times 10^{-9}$ Pa.m.s, which is an order of magnitude lower than typical values reported in the literature (see Table 1). As only a finite number of values were tested, this value should just be considered as an order of magnitude for effective membrane viscosity in the simulated regime.

To the best of our knowledge, this is the first time that RBC membrane viscosity values have been estimated in conditions where RBCs are subjected to strain rates (norm of the strain-rate tensor) on the order of 10^5- 10^6 s^{-1}, which are found of the ABX Micros 60 analyzer. Most measurements used to assess η_{memb} have been conducted at significantly lower shear rates. For example, the shear rates applied in the tank-treading experiments by Tran-Son-Tay *et al.*[30] are on the order of $1 - 100$ s^{-1}. While unmodeled phenomena - electric field effects - may influence the predictions, the discrepancy between our estimated viscosity values and those commonly reported in the literature may also be due to a shear-thinning behavior of the RBC membrane, also reported in other studies[31,30].

Although further efforts are needed to calibrate η_{memb}, our study demonstrates that RBCs sphericity, membrane viscosity, cytoplasmic viscosity, and its initial orientation when entering the orifice, play a key role in capturing the wide range of pulse shapes observed in the experiments. In contrast, in the range considered (from 2.2 to 22.5 $\mu N.m^{-1}$) the membrane shear modulus plays a secondary role in this configuration. However, some pathological conditions can result in significantly higher values. For instance, in some cases of aging, sickle cell disease, ovalocytosis, or malaria, values of G_s as high as 60 $\mu N.m^{-1}$ have been reported[60,61,62]. In such cases, the RBC shear modulus may have a measurable impact on the pulses.

This study did not explore the full parameter space of the model. Parameters that had only a minor influence on the electric signal in preliminary tests, such as the bending modulus, area dilatation modulus, and spontaneous curvature, were held constant. While these parameters may affect RBC deformation dynamics, our focus was on the electric signal, which is the sole experimental observable in this work. In particular, all simulations assumed RBCs with zero spontaneous curvature. Future work could extend the analysis by introducing non-zero spontaneous curvature in the Helfrich bending energy or adopting more

sophisticated energy formulations[51], enabling the study of alternative RBC shapes, such as stomatocytes or echinocytes, and their impact on the electric signal.

An important limitation of the model itself is the potential for RBC damage. It is well established that RBCs tolerate high stresses without damage only when exposure times are sufficiently short. Classical studies report hemolysis under prolonged exposure to high shear stresses[33], while more recent works have demonstrated sub-lethal alterations in deformability at lower shear levels and/or shorter exposures[34]. In our configuration, RBCs locally experience high stresses ($\approx$ 100–200 Pa), but only for very brief transit times (on the order of tens of microseconds). To the best of our knowledge, this short-duration/high-stress regime has not been characterized in the literature with respect to blood damage. As a result, sub-lethal mechanical effects cannot be excluded. In our experiments, destruction of the RBCs would manifest as detectable changes in the electrical signal, which have not been observed. However, more subtle alterations (e.g., decreased deformability or membrane changes) may occur and could bias the inference of RBC properties, as damage-induced changes are not accounted for in the current model. Future work should address this limitation by explicitly incorporating RBC damage into the inference framework or by exploring lower-stress operating regimes. In particular, comparing inferred RBC parameters across varying throughputs (and thus stresses) would help identify stress thresholds beyond which mechanical damage begins to bias inferred RBC properties.

5 | CONCLUSIONS

In this paper, we propose a numerical approach to investigate the effects of RBC properties on the impedance pulses generated in a Coulter counter (CC) during blood analysis, with the long-term aim of extending its diagnostic capabilities to the morphological and rheological assessment of RBCs. Compared to existing numerical methods, the computational gains enabled by the MA algorithm introduced here allows us to significantly increase the number of operating points considered. This enables a sensitivity analysis of impedance pulses with respect to a broad set of RBC parameters, including factors not previously considered in this context, such as membrane viscosity.

Our numerical study, focused on healthy blood samples, confirms the influence of both morphological and rheological RBC properties on pulse shape. By comparing our results with experimental data, we identify cell sphericity, membrane viscosity, and cytoplasmic viscosity as primary contributors to the observed variability in the pulse shapes predicted by the model. In addition, we discovered that for rigid RBCs, their orientation relative to the flow direction plays a significant role — a finding not previously reported.

Nevertheless, only three discrete levels were tested for each parameter, and interactions between parameters were not fully investigated. Future work will include a more comprehensive sensitivity analysis to fully evaluate the combined effects of RBC properties on pulses. Furthermore, we will extend this study by including multiple RBC trajectories around the single one considered in this study. This generalization is expected to offer a more robust and insightful evaluation of the influence of RBC parameters on CC measurements.

Finally, to improve the inference of RBC properties from experimental measurements, future work may require refinements to the model or experimental setup to better align with real-world conditions.

AUTHOR CONTRIBUTIONS

Conceptualization: Pierre Pottier | Pierre Taraconat | Damien Isèbe | Franck Nicoud | Simon Mendez
Formal Analysis: Pierre Pottier
Investigation: Pierre Pottier | Pierre Taraconat | Jean-Philippe Gineys
Methodology: Pierre Pottier | Pierre Taraconat | Damien Isèbe | Franck Nicoud | Simon Mendez
Resources: Pierre Taraconat | Jean-Philippe Gineys | Simon Mendez
Software: Pierre Pottier | Franck Nicoud | Simon Mendez
Writing - Original Draft Preparation: Pierre Pottier
Writing - Review & Editing: Pierre Taraconat | Jean-Philippe Gineys | Damien Isèbe | Franck Nicoud | Simon Mendez

ACKNOWLEDGMENTS

This work was carried out using the YALES2 and YALES2BIO computational frameworks - YALES2BIO is developed on the basis of YALES2. The authors gratefully acknowledge the developers and maintainers of both YALES2 and YALES2BIO for providing the tools that enabled the high-fidelity simulations presented in this study.

CFD simulations were performed using HPC resources from GENCI-TGCC (Grants No. A0140307194 to A0180307194) and from the Institut de Sciences des Données de Montpellier (ISDM).

FINANCIAL DISCLOSURE

None reported.

CONFLICT OF INTEREST

The authors declare no potential conflict of interests.

REFERENCES

1. Cho YI, Mooney MP, Cho DJ. Hemorheological Disorders in Diabetes Mellitus. *Journal of diabetes science and technology (Online).* 2008;2(6):1130–1138.
2. Cynober T, Mohandas N, Tchernia G. Red Cell Abnormalities in Hereditary Spherocytosis: Relevance to Diagnosis and Understanding of the Variable Expression of Clinical Severity. *Journal of Laboratory and Clinical Medicine.* 1996;128(3):259–269. doi: 10.1016/S0022-2143(96)90027-X
3. Llaudet-Planas E, Vives-Corrons JL, Rizzuto V, et al. Osmotic Gradient Ektacytometry: A Valuable Screening Test for Hereditary Spherocytosis and Other Red Blood Cell Membrane Disorders. *International Journal of Laboratory Hematology.* 2018;40(1):94–102. doi: 10.1111/ijlh.12746
4. Brandão MM, Fontes A, Barjas-Castro ML, et al. Optical Tweezers for Measuring Red Blood Cell Elasticity: Application to the Study of Drug Response in Sickle Cell Disease. *European Journal of Haematology.* 2003;70(4):207–211. doi: 10.1034/j.1600-0609.2003.00027.x
5. Itoh T, Chien S, Usami S. Effects of Hemoglobin Concentration on Deformability of Individual Sickle Cells after Deoxygenation. *Blood.* 1995;85(8):2245–2253. doi: 10.1182/blood.V85.8.2245.bloodjournal8582245
6. Bourguignon C, Ansel C, Gineys JP, et al. New Erythrocyte Parameters Derived from the Coulter Principle Relate with Red Blood Cell Properties—A Pilot Study in Diabetes Mellitus. *PLOS ONE.* 2023;18(10):e0293356. doi: 10.1371/journal.pone.0293356
7. Lelièvre JC, Bucherer C, Geiger S, Lacombe C, Vereycken V. Blood Cell Biomechanics Evaluated by the Single-Cell Micromanipulation. *Journal de Physique III.* 1995;5(10):1689–1706. doi: 10.1051/jp3:1995218
8. Evans E. New Membrane Concept Applied to the Analysis of Fluid Shear- and Micropipette-Deformed Red Blood Cells. *Biophysical Journal.* 1973;13(9):941–954. doi: 10.1016/S0006-3495(73)86036-9
9. Song H, Liu Y, Zhang B, et al. Study of in Vitro RBCs Membrane Elasticity with AOD Scanning Optical Tweezers. *Biomedical Optics Express.* 2017;8(1):384. doi: 10.1364/BOE.8.000384
10. Hénon S, Lenormand G, Richert A, Gallet F. A New Determination of the Shear Modulus of the Human Erythrocyte Membrane Using Optical Tweezers. *Biophysical Journal.* 1999;76(2):1145–1151. doi: 10.1016/S0006-3495(99)77279-6
11. Dulińska I, Targosz M, Strojny W, et al. Stiffness of Normal and Pathological Erythrocytes Studied by Means of Atomic Force Microscopy. *Journal of Biochemical and Biophysical Methods.* 2006;66(1):1–11. doi: 10.1016/j.jbbm.2005.11.003
12. Chen X, Feng L, Jin H, Feng S, Yu Y. Quantification of the Erythrocyte Deformability Using Atomic Force Microscopy: Correlation Study of the Erythrocyte Deformability with Atomic Force Microscopy and Hemorheology. *Clinical Hemorheology and Microcirculation.* 2009;43(3):241–249. doi: 10.3233/CH-2009-1234
13. Rab MAE, Kanne CK, Boisson C, et al. Oxygen Gradient Ektacytometry–Derived Biomarkers Are Associated with Acute Complications in Sickle Cell Disease. *Blood Advances.* 2024;8(2):276–286. doi: 10.1182/bloodadvances.2023011013
14. Tomaiuolo G, Barra M, Preziosi V, Cassinese A, Rotoli B, Guido S. Microfluidics Analysis of Red Blood Cell Membrane Viscoelasticity. *Lab Chip.* 2011;11(3):449–454. doi: 10.1039/C0LC00348D
15. Saadat A, Huyke DA, Oyarzun DI, et al. A System for the High-Throughput Measurement of the Shear Modulus Distribution of Human Red Blood Cells. *Lab on a Chip.* 2020;20(16):2927–2936. doi: 10.1039/D0LC00283F
16. Bianchi P, Van Wijk R. Editorial: New Methods for Red Blood Cell Research and Diagnosis. *Frontiers in Physiology.* 2021;12:755664. doi: 10.3389/fphys.2021.755664
17. Risinger M, Kalfa TA. Red Cell Membrane Disorders: Structure Meets Function. *Blood.* 2020;136(11):1250–1261. doi: 10.1182/blood.2019000946
18. Coulter WH. Means for Counting Particles Suspended in a Fluid US2656508A. https://patentimages.storage.googleapis.com/1e/be/f1/724ae3a4ad7d5d/US2656508 1953.
19. Taraconat P, Gineys JP, Isebe D, Nicoud F, Mendez S. Numerical Simulation of Deformable Particles in a Coulter Counter. *International Journal for Numerical Methods in Biomedical Engineering.* 2019;35(11). doi: 10.1002/cnm.3243
20. Kachel V. Sizing of Cells by the Electrical Resistance Pulse Technique: Methodology and Application in Cytometric Systems. In: Catsimpoolas N., ed. *Cell Analysis*, , Boston, MA: Springer US, 1982:195–331
21. Golibersuch D. Observation of Aspherical Particle Rotation in Poiseuille Flow via the Resistance Pulse Technique. *Biophysical Journal.* 1973;13(3):265–280. doi: 10.1016/S0006-3495(73)85984-3
22. Waterman CS, Atkinson EE, Wilkins B, Fischer CL, Kimzey SL. Improved Measurement of Erythrocyte Volume Distribution by Aperture-Counter Signal Analysis. *Clinical Chemistry.* 1975;21(9):1201–1211. doi: 10.1093/clinchem/21.9.1201
23. Tatsumi N, Tsuda I, Fujimoto K, Matsumoto H. Evaluation of a New Blood Cell Counter with Sheath Flow System. *Cytometry.* 1985;6(5):395–400. doi: 10.1002/cyto.990060502
24. Taraconat P, Gineys JP, Isèbe D, Nicoud F, Mendez S. Detecting Cells Rotations for Increasing the Robustness of Cell Sizing by Impedance Measurements, with or without Machine Learning. *Cytometry Part A.* 2021;99(10):977–986. doi: 10.1002/cyto.a.24356
25. Taraconat P, Gineys JP, Isebe D, Nicoud F, Mendez S. Red Blood Cell Rheology during a Complete Blood Count: A Proof of Concept. *PLOS ONE.* 2023;18(1):e0280952. doi: 10.1371/journal.pone.0280952
26. Mendez S, Gibaud E, Nicoud F. An Unstructured Solver for Simulations of Deformable Particles in Flows at Arbitrary Reynolds Numbers. *Journal of Computational Physics.* 2014;256:465–483. doi: 10.1016/j.jcp.2013.08.061
27. Skalak R, Tozeren A, Zarda R, Chien S. Strain Energy Function of Red Blood Cell Membranes. *Biophysical Journal.* 1973;13(3):245–264. doi: 10.1016/S0006-3495(73)85983-1

28. Helfrich W. Elastic Properties of Lipid Bilayers: Theory and Possible Experiments. *Zeitschrift für Naturforschung C.* 1973;28(11-12):693–703. doi: 10.1515/znc-1973-11-1209
29. Hochmuth R, Worthy P, Evans E. Red Cell Extensional Recovery and the Determination of Membrane Viscosity. *Biophysical Journal.* 1979;26(1):101–114. doi: 10.1016/S0006-3495(79)85238-8
30. Tran-Son-Tay R, Sutera SP, Rao PR. Determination of Red Blood Cell Membrane Viscosity from Rheoscopic Observations of Tank-Treading Motion. *Biophysical Journal.* 1984;46(1):65–72. doi: 10.1016/S0006-3495(84)83999-5
31. Matteoli P, Nicoud F, Mendez S. Impact of the Membrane Viscosity on the Tank-Treading Behavior of Red Blood Cells. *Physical Review Fluids.* 2021;6(4):043602. doi: 10.1103/PhysRevFluids.6.043602
32. Yazdani A, Bagchi P. Influence of Membrane Viscosity on Capsule Dynamics in Shear Flow. *Journal of Fluid Mechanics.* 2013;718:569–595. doi: 10.1017/jfm.2012.637
33. Leverett LB, Hellums JD, Alfrey CP, Lynch EC. Red Blood Cell Damage by Shear Stress. *Biophysical Journal.* 1972;12(3):257–273. doi: 10.1016/S0006-3495(72)86085-5
34. Horobin JT, Sabapathy S, Simmonds MJ. Red Blood Cell Tolerance to Shear Stress above and below the Subhemolytic Threshold. *Biomechanics and Modeling in Mechanobiology.* 2020;19(3):851–860. doi: 10.1007/s10237-019-01252-z
35. Peskin CS. The Immersed Boundary Method. *Acta Numerica.* 2002;11:479–517. doi: 10.1017/S0962492902000077
36. Liu WK, Jun S, Zhang YF. Reproducing kernel particle methods. *International Journal for Numerical Methods in Fluids.* 1995;20(8-9):1081–1106. doi: 10.1002/fld.1650200824
37. Charrier JM, Shrivastava S, Wu R. Free and Constrained Inflation of Elastic Membranes in Relation to Thermoforming — Axisymmetric Problems. *The Journal of Strain Analysis for Engineering Design.* 1987;22(2):115–125. doi: 10.1243/03093247V222115
38. Zhong-can OY, Helfrich W. Bending Energy of Vesicle Membranes: General Expressions for the First, Second, and Third Variation of the Shape Energy and Applications to Spheres and Cylinders. *Physical Review A.* 1989;39(10):5280–5288. doi: 10.1103/PhysRevA.39.5280
39. Chorin AJ. Numerical Solution of the Navier-Stokes Equations. *Mathematics of Computation.* 1968;22(104):745–762. doi: 10.1090/S0025-5718-1968-0242392-2
40. Malandain M, Maheu N, Moureau V. Optimization of the Deflated Conjugate Gradient Algorithm for the Solving of Elliptic Equations on Massively Parallel Machines. *Journal of Computational Physics.* 2013;238:32–47. doi: 10.1016/j.jcp.2012.11.046
41. Briole A, Podgorski T, Abou B. Molecular Rotors as Intracellular Probes of Red Blood Cell Stiffness. *Soft Matter.* 2021;17(17):4525–4537. doi: 10.1039/D1SM00321F
42. Kelemen C, Chien S, Artmann GM. Temperature Transition of Human Hemoglobin at Body Temperature: Effects of Calcium. *Biophysical Journal.* 2001;80(6):2622–2630. doi: 10.1016/S0006-3495(01)76232-7
43. Monkos K, Turczynski B. Determination of the Axial Ratio of Globular Proteins in Aqueous Solution Using Viscometric Measurements. *International Journal of Biological Macromolecules.* 1991;13(6):341–344. doi: 10.1016/0141-8130(91)90015-M
44. Waugh R, Narla M, Jackson C, Mueller T, Suzuki T, Dale G. Rheologic Properties of Senescent Erythrocytes: Loss of Surface Area and Volume with Red Blood Cell Age. *Blood.* 1992;79(5):1351–1358. doi: 10.1182/blood.V79.5.1351.1351
45. Linderkamp O, Meiselman HJ. Geometric, Osmotic, and Membrane Mechanical Properties of Density-Separated Human Red Cells. *Blood.* 1982;59(6):1121–1127. doi: 10.1182/blood.V59.6.1121.1121
46. Park H, Lee S, Ji M, et al. Measuring Cell Surface Area and Deformability of Individual Human Red Blood Cells over Blood Storage Using Quantitative Phase Imaging. *Scientific Reports.* 2016;6(1):34257. doi: 10.1038/srep34257
47. Guglietta F, Behr M, Biferale L, Falcucci G, Sbragaglia M. On the Effects of Membrane Viscosity on Transient Red Blood Cell Dynamics. *Soft Matter.* 2020;16(26):6191–6205. doi: 10.1039/D0SM00587H
48. Evans E, Waugh R, Melnik L. Elastic Area Compressibility Modulus of Red Cell Membrane. *Biophysical Journal.* 1976;16(6):585–595. doi: 10.1016/S0006-3495(76)85713-X
49. Cordasco D, Bagchi P. Intermittency and Synchronized Motion of Red Blood Cell Dynamics in Shear Flow. *Journal of Fluid Mechanics.* 2014;759:472–488. doi: 10.1017/jfm.2014.587
50. Grover NB, Naaman J, Ben-Sasson S, Doljanski F. Electrical Sizing of Particles in Suspensions: III. Rigid Spheroids and Red Blood Cells. *Biophysical Journal.* 1972;12(9):1099–1116. doi: 10.1016/S0006-3495(72)86147-2
51. Lim H. W. G, Wortis M, Mukhopadhyay R. Stomatocyte–Discocyte–Echinocyte Sequence of the Human Red Blood Cell: Evidence for the Bilayer– Couple Hypothesis from Membrane Mechanics. *Proceedings of the National Academy of Sciences.* 2002;99(26):16766–16769. doi: 10.1073/pnas.202617299
52. Grenouilloux A, Bechane Y, Carmona J, et al. *High-Fidelity Simulation of the Aerothermal Performances of a Turbofan Thrust Reverser*. PhD thesis. American Society of Mechanical Engineers, London, United Kingdom; 2024.
53. Dobrzynski C, Frey P. Anisotropic Delaunay Mesh Adaptation for Unsteady Simulations. In: Garimella RV., ed. *Proceedings of the 17th International Meshing Roundtable*, , Berlin, Heidelberg: Springer Berlin Heidelberg, 2008:177–194
54. Dapogny C, Dobrzynski C, Frey P. Three-Dimensional Adaptive Domain Remeshing, Implicit Domain Meshing, and Applications to Free and Moving Boundary Problems. *Journal of Computational Physics.* 2014;262:358–378. doi: 10.1016/j.jcp.2014.01.005
55. Bénard P. *Analyse et amélioration d'une chambre de combustion centimétrique par simulations aux grandes échelles*. PhD thesis. INSA de Rouen, Rouen, France; 2015.
56. Akeson S, Mel H. Erythrocyte and Ghost Cytoplasmic Resistivity and Voltage-Dependent Apparent Size. *Biophysical Journal.* 1983;44(3):397–403. doi: 10.1016/S0006-3495(83)84313-6
57. Nodargi NA, Bisegna P, Caselli F. Effective Computational Modeling of Erythrocyte Electro-Deformation. *Meccanica.* 2017;52(3):613–631. doi: 10.1007/s11012-016-0424-0
58. Qiang Y, Liu J, Du E. Dielectrophoresis Testing of Nonlinear Viscoelastic Behaviors of Human Red Blood Cells. *Micromachines.* 2018;9(1):21. doi: 10.3390/mi9010021
59. Di Pietro DA, Mendez S, Spadotto AE. A Discrete de Rham Discretization of Interface Diffusion Problems with Application to the Leaky Dielectric Model. *Journal of Computational Physics.* 2025;530:113920. doi: 10.1016/j.jcp.2025.113920
60. Evans E, Mohandas N. Membrane-Associated Sickle Hemoglobin: A Major Determinant of Sickle Erythrocyte Rigidity. *Blood.* 1987;70(5):1443–1449. doi: 10.1182/blood.V70.5.1443.1443

61. Nash GB, O'Brien E, Gordon-Smith EC, Dormandy JA. Abnormalities in the Mechanical Properties of Red Blood Cells Caused by Plasmodium Falciparum. *Blood.* 1989;74(2):855–861. doi: 10.1182/blood.V74.2.855.855
62. Suresh S. Mechanical Response of Human Red Blood Cells in Health and Disease: Some Structure-Property-Function Relationships. *Journal of Materials Research.* 2006;21(8):1871–1877. doi: 10.1557/jmr.2006.0260